



**HAL**  
open science

## **p-Type Ultrawide-Band-Gap Spinel ZnGa<sub>2</sub>O<sub>4</sub>: New Perspectives for Energy Electronics**

Ekaterine Chikoidze, Corinne Sartel, Ismail Madaci, Hagar Mohamed, Christèle Vilar, Belén Ballesteros, Francisco Belarre, Elena del Corro, Pablo Vales-Castro, Guillaume Sauthier, et al.

► **To cite this version:**

Ekaterine Chikoidze, Corinne Sartel, Ismail Madaci, Hagar Mohamed, Christèle Vilar, et al.. p-Type Ultrawide-Band-Gap Spinel ZnGa<sub>2</sub>O<sub>4</sub>: New Perspectives for Energy Electronics. *Crystal Growth & Design*, 2020, 20 (4), pp.2535-2546. 10.1021/acs.cgd.9b01669 . hal-02615181

**HAL Id: hal-02615181**

**<https://hal.science/hal-02615181v1>**

Submitted on 23 Nov 2020

**HAL** is a multi-disciplinary open access archive for the deposit and dissemination of scientific research documents, whether they are published or not. The documents may come from teaching and research institutions in France or abroad, or from public or private research centers.

L'archive ouverte pluridisciplinaire **HAL**, est destinée au dépôt et à la diffusion de documents scientifiques de niveau recherche, publiés ou non, émanant des établissements d'enseignement et de recherche français ou étrangers, des laboratoires publics ou privés.

# ***P*-type ultra-wide bandgap spinel ZnGa<sub>2</sub>O<sub>4</sub>: new perspectives for energy electronics**

*Ekaterine Chikoidze*<sup>\*1</sup>, *Corinne Sartel*<sup>1</sup>, *Ismail Madaci*<sup>1</sup>, *Hagar Mohamed*<sup>1,2</sup>, *Christele. Villar*<sup>1</sup>, *Belén Ballesteros*<sup>3</sup>, *Francisco Belarre*<sup>3</sup>, *Elena del Corro*<sup>3</sup>, *Pablo Vales-Castro*<sup>3</sup>, *Guillaume Sauthier*<sup>3</sup>, *Lijie Li*<sup>4</sup>, *Mike Jennings*<sup>4</sup>, *Vincent Sallet*<sup>1</sup>, *Yves Dumont*<sup>1</sup> and *Amador Pérez-Tomás*<sup>\*3</sup>

<sup>1</sup>Groupe d'Etude de la Matière Condensée (GEMaC), Université de Versailles Saint Quentin en Y. – CNRS, Université Paris-Saclay, 45 Av. des Etats-Unis, 78035 Versailles Cedex, France.

<sup>2</sup>Solid State Physics Department, National Research Center, El-Behooth St. 12311 Dokki, Giza, Egypt.

<sup>3</sup>Catalan Institute of Nanoscience and Nanotechnology (ICN2), CSIC and The Barcelona Institute of Science and Technology, Barcelona, Spain.

<sup>4</sup> College of Engineering, Swansea University, Bay Campus, Fabian Way, Crymlyn Burrows, Swansea, SA1 8EN, UK.

**e-mail:** [ekaterine.chikoidze@uvsq.fr](mailto:ekaterine.chikoidze@uvsq.fr); [amador.perez@icn2.cat](mailto:amador.perez@icn2.cat)

**Keywords:** Ultra-wide Bandgap Semiconductor, Spinel Oxides, ZnGa<sub>2</sub>O<sub>4</sub>, *p*-type Conductivity

## Abstract

The family of spinel compounds is a large and important class of multi-functional materials of general formulation  $AB_2X_4$  with many advanced applications in energy and optoelectronic areas such fuel cells, batteries, catalysis, photonics, spintronics or thermoelectricity. In this work, it is demonstrated that the ternary ultra-wide band gap ( $\sim 5$  eV) spinel zinc gallate ( $ZnGa_2O_4$ ) arguably is the native  $p$ -type ternary oxide semiconductor with the largest  $E_g$ , (in pair with recently discovered binary  $p$ -type monoclinic  $\beta$ - $Ga_2O_3$  oxide). For nominally undoped  $ZnGa_2O_4$  high temperature Hall effect hole concentration was determined to be as large as  $p = 2 \times 10^{15} \text{ cm}^{-3}$  while hole mobilities were found to be  $\mu_h = 7\text{-}10 \text{ cm}^2/\text{Vs}$  (in the 680-850 K temperature range). An acceptor-like small Fermi level was further corroborated by x-ray spectroscopy and by density functional theory calculations. Our findings, as an important step towards  $p$ -type doping, opens up further perspectives for ultra-wide bandgap *bipolar spinel electronics* and further promotes ultra-wide bandgap ternary oxides such as  $ZnGa_2O_4$  to the forefront of the quest of the next generation of semiconductor materials for more efficient energy optoelectronics and power electronics.

## 1. Introduction

Ultra-wide bandgap semiconductor oxides<sup>[1,2]</sup> are a class of materials that currently are attracting a lot of attention as an emerging multi-functional platform owing to their unusual material properties<sup>[3-5]</sup>, endurance (high critical fields, radiation hardness, etc)<sup>[6-9]</sup> and unique optoelectronic properties<sup>[10-12]</sup>. The emerging transparent semiconductor oxide (TSO) technology based on ultra-wide bandgap oxides holds the promise of extending many energy and optoelectronic applications further into the deep ultraviolet range, surpassing the conventional wide bandgap TSO's near ultraviolet limit ( $\sim 3.5$  eV) (e.g. ZnO, SnO<sub>2</sub> or In<sub>2</sub>O<sub>3</sub>)<sup>[13-15]</sup>. Nevertheless, to exploit the full potential of any emerging ultra-wide bandgap solid-state semiconductor technology for electronics, a good control (over several orders of magnitude) of the *n*-type and *p*-type conductivity should be attained.

Recently, single crystal *n*-type gallium oxide (Ga<sub>2</sub>O<sub>3</sub>) and zinc gallate (ZnGa<sub>2</sub>O<sub>4</sub>) are being revisited as ultra-wide bandgap ( $\sim 5$  eV) oxide semiconductors. In particular, some very recent works such as the ones from Hrong *et al.*<sup>[11]</sup> and Galazka *et al.*<sup>[16]</sup> have evidenced the great prospects of *n*-type ZnGa<sub>2</sub>O<sub>4</sub> as potential semiconductor platform for future ultra-wide bandgap oxide optoelectronics<sup>[17]</sup>. In this work, we show that engineered ZnGa<sub>2</sub>O<sub>4</sub> epitaxial single crystal layers may also be an ultra wide bandgap native *p*-type semiconductor with great dopability prospects owing to the spinel's inherent diversity of choices of cation coordination<sup>[18-19]</sup>. Spinels generally refer to compounds with formulation AB<sub>2</sub>X<sub>4</sub> where A<sup>2+</sup> is a divalent cation such as Zn, Ni, Cu, Sn, Mg, Cr, Mn, Fe, Co or Cd, B<sup>3+</sup> is a trivalent cation such as Ga, Al, In, Ti, V, Fe, Co, Ni, V, Cr, Mn and X<sup>2-</sup> is a divalent anion such as O, S or Se<sup>[20]</sup>. There are over 1,000

known compounds that crystalize in the spinel structure and the sub-family of spinel oxides is a large and important class of multi-functional oxide semiconductors with many energy optoelectronics applications [21–23] in areas such batteries [24,25], fuel cells [26], catalysis (water splitting<sup>[27,28]</sup>, photocatalysis [29,30]), photonics (phosphors [31–33], bio-imaging [34,35], transparent electrodes<sup>[36]</sup>, photodetectors [37,38]), spintronics (magnets<sup>[39]</sup>, bio-magnets<sup>[40]</sup>) or thermoelectricity [41]. Normal spinels have all A cations in the tetrahedral site and all B cations in the octahedral site, e.g. Zn-tetrahedral site  $\text{Zn}^{2+}(\text{T}_d)$  and Ga-octahedral site  $\text{Ga}^{3+}(\text{O}_h)$  so that normal  $\text{ZnGa}_2\text{O}_4$  is  $\text{Zn}^{2+}(\text{T}_d)\text{Ga}_2(\text{O}_h)\text{O}_4^{2-}$ . The spinel's off-stoichiometry, which leads to a deviation from the ideal 1:2:4 stoichiometry, or the creation of cation antisite defects are known routes for doping these compounds. Dominant defects in spinels are antisite acceptors (e.g.  $\text{Zn}_{\text{Ga}}$ ) with acceptor-like  $\text{Zn}^{2+}(\text{T}_d)\text{-on-O}_h$  antisite defects or donor-like  $\text{Ga}^{3+}(\text{O}_h)\text{-on-T}_d$  as  $\text{Ga}_{\text{Zn}}$  defects<sup>[42–46]</sup>. Although spinel's dopability was already predicted, experimentally demonstrated on very few visible transparent (i.e.  $E_g \sim 3$  eV) oxide spinels (e.g.  $\text{ZnRh}_2\text{O}_4$  or  $\text{ZnIr}_2\text{O}_4$ )<sup>[47,48]</sup>, and virtually no direct evidence of *p*-type conductivity (only indirectly by Hrong *et al.*<sup>[49]</sup> to the best of our knowledge) has been reported for UWBG spinel's yet. It is worth mentioning that acceptor doping in other ultra-wide band gap (UWBG) non-spinel oxides such as monoclinic  $\beta\text{-Ga}_2\text{O}_3$  is also still challenging<sup>[50],[51]</sup>. Therefore, the new prospects opening up by *p*-type ternaries such as  $\text{ZnGa}_2\text{O}_4$  may represent a good opportunity to mitigate the acceptor issue in binary UWBGs. To achieve efficient *p*-type doping in wide band gap materials, we believe that the first step is the realization of undoped semiconductor with hole conductivity originated from native acceptor defects. It is clear that such semiconductor should be in off-stoichiometric state, but due to deep acceptor centre levels it will be highly resistive. Following this approach, the goal of the work was fabrication of undoped  $\text{ZnGa}_2\text{O}_4$  with native hole conductivity. By demonstrating the intrinsic *p*-type behaviour of the ultra-wide bandgap  $\text{ZnGa}_2\text{O}_4$  we make feasible the predicted *p*-type doping, which paves

the way to bipolar ultra-wide bandgap *spinel electronics* for a range of emerging power and energy optoelectronic applications.

What does bipolar ultra-wide bandgap *spinel electronics* would mean? Oxide electronics is currently based on classic and very well-known binary oxide semiconductors while emerging applications mostly rely on complex oxides. Binary oxide examples include  $\text{CuO}_2$  for photovoltaics,  $\text{In}_2\text{O}_3$ ,  $\text{SnO}_2$  and  $\text{ZnO}$  for transparent electronics and, recently,  $\text{Ga}_2\text{O}_3$  has disrupted for power and UV opto-electronics. Owing to the flatness of the oxygen-related valence band and the deep energy of acceptor extrinsic dopant atoms, the hole conductivity of wide- and ultra-wide binary oxides it is well-known to be very challenging. Therefore, electronic devices made of these binary WBG semiconductors are mostly unipolar and *n*-type. Among complex oxides, ternary perovskite oxides, (with general formulation  $\text{ABO}_3$ ), is perhaps the most common platform of choice for advanced oxide electronics. Perovskite oxides, while exhibiting a range of complementary properties such as ferroelectricity, colossal magnetoresistance or anomalous conducting interfaces (e.g.  $\text{SrTiO}_3/\text{LaAlO}_3$ ) still have not been demonstrated to deliver any competitive advantage for energy or power electronics due to their relative low bandgap ( $\sim 3$  eV) and modest dielectric breakdown field. Here, it is demonstrated that spinel  $\text{ZnGa}_2\text{O}_4$  may be a native *p*-type ultra-wide bandgap semiconductor ( $\sim 5$  eV). Hence, spinel oxides (a large family of  $\text{AB}_2\text{O}_4$  compounds mostly unexplored as wide bandgap power semiconductors) may represent a brand new opportunity for bipolar oxide energy electronics (i.e., for managing large quantities of switching electrical energy) as they would join the required qualities of sustaining large electrical fields in *p-n* junctions in the off-state together with low losses in the on-state. The prospects of growing spinel  $\text{ZnGa}_2\text{O}_4$  with high quality, either, as thin-film onto cheap sapphire substrates or as a single-crystal (in a fashion similar to  $\beta\text{-Ga}_2\text{O}_3$ ) would make this approach feasible. Further,  $\text{ZnGa}_2\text{O}_4$  may represent an unprecedented energy electronic platform for futuristic

energy generation, storage and power system integration since oxide spinels have been demonstrated as excellent phosphors, magnets, fuel cell and battery electrodes thus suggesting a promising and yet fairly unexplored smart integrated energy systems for the internet of things.

### **1. From Ga<sub>2</sub>O<sub>3</sub>/ZnGa<sub>2</sub>O<sub>4</sub> mixed phases to monophase ZnGa<sub>2</sub>O<sub>4</sub>**

In this experiment, the spinel's ZnGa<sub>2</sub>O<sub>4</sub> stoichiometry and its structural morphology have been optimized within a metalorganic chemical vapor deposition (MOCVD) chamber during the growth of strongly compensated *p*-type  $\beta$ -Ga<sub>2</sub>O<sub>3</sub> [51] in a progressively richer Zn-ambient. The ZnGa<sub>2</sub>O<sub>4</sub> samples were grown in a RF-heated horizontal MOCVD reactor on *c*-oriented sapphire (Al<sub>2</sub>O<sub>3</sub>) substrates, as described in the experimental section. In short, during the growth, the flow rate of the gallium precursors and oxygen were kept at 11  $\mu$ mol/min and 1200 sccm respectively. The growth temperature, pressure and time were set at 775°C, 38 torr 150 minutes, respectively. Then, a number of Ga-Zn-O samples were grown varying the Zn-flux (diethylzinc (DEZn)) in the range of 0-9  $\mu$ mol/min. Pure  $\beta$ -Ga<sub>2</sub>O<sub>3</sub> was grown at a Zn-flux of 0  $\mu$ mol/min (termed Zn-0), while, for simplicity, in the following, the analysis is restricted to the most representative Zn-fluxes of 3,9  $\mu$ mol/min (Zn-4), 7  $\mu$ mol/min (Zn-7) and 8,9  $\mu$ mol/min (Zn-9). The Ga-Zn-O layer thickness (ranging 900 to 1200 nm) was determined by cross-sectional scanning electron microscope (SEM) and transmission electron microscopy (TEM), as described in Methods.

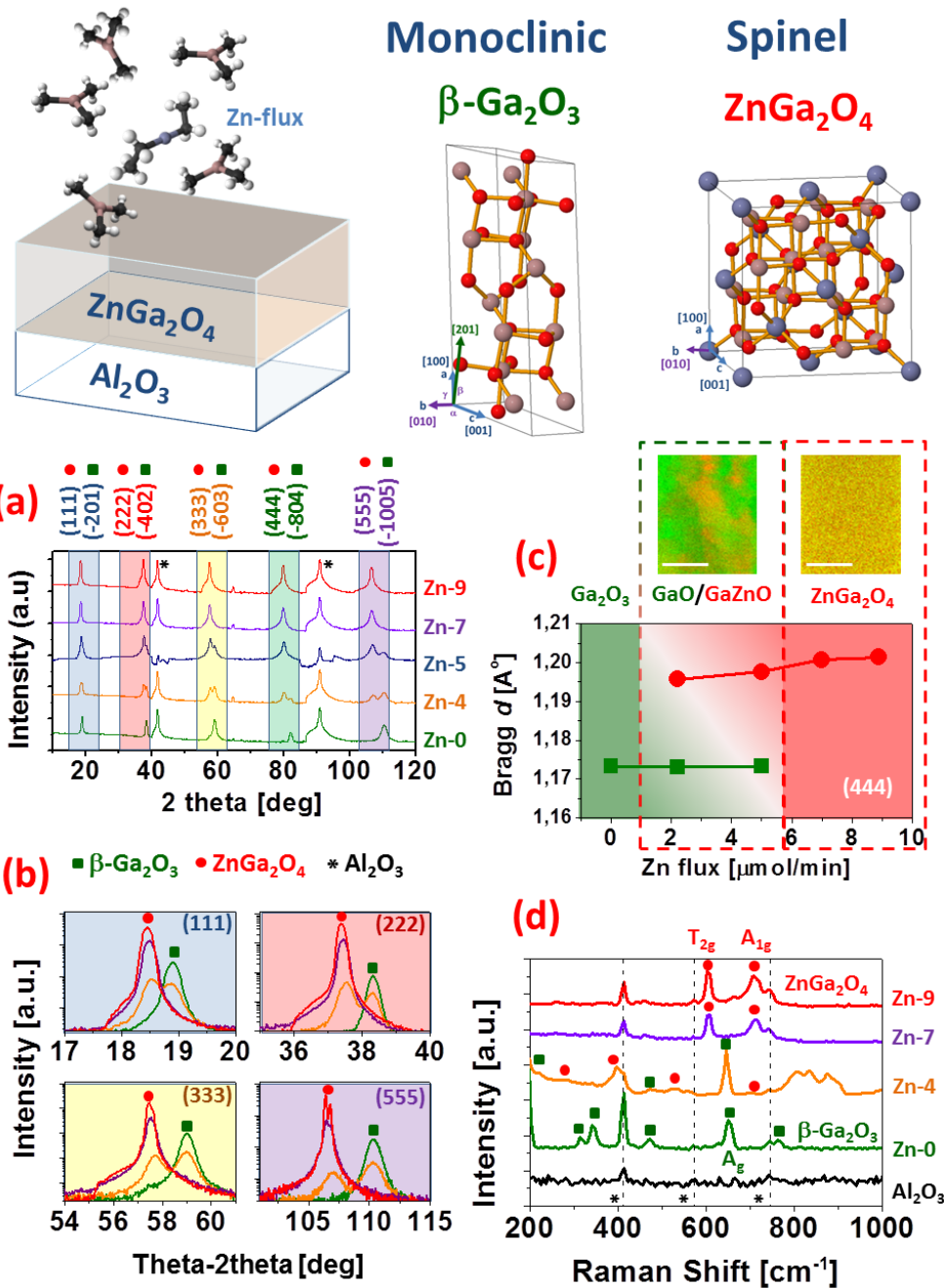


**Figure 1.** (a) Full XRD pattern for  $\beta\text{-Ga}_2\text{O}_3$  and Ga-Zn-O thin-films with increasing Zn incorporation (Zn-flux [ $\mu\text{mol}/\text{min}$ ] Zn-0, Zn-4, Zn-5, Zn-7, Zn-9). (b) An enlarged view of 4 peaks at  $2\theta=18.91^\circ$ ,  $38.32^\circ$ ,  $58.99^\circ$  and  $110.29^\circ$  to show the phase transition from monoclinic  $\beta\text{-Ga}_2\text{O}_3$  to  $\text{ZnGa}_2\text{O}_4$  spinel phase. For low Zn-flux, the Ga-Zn-O layers show a double peak feature of mixed phases (GaO/GaZnO) of pure  $\beta$ -



Ga<sub>2</sub>O<sub>3</sub> (GaO) and pure ZnGa<sub>2</sub>O<sub>4</sub>. (c) Bragg distance as a function of Zn-flux from the (-804)/(444) reflection in the GaO, mixed phase GaO/GaZnO and pure spinel ZnGa<sub>2</sub>O<sub>4</sub> region. The inset in (c) are from Zn-4 and Zn-9 2D composition maps from transmission microscopy (TEM) electron energy loss spectroscopy (EELS) which further corroborates the mixed phase region and the pure ZnGa<sub>2</sub>O<sub>4</sub> regions (white scale bar is 100 nm). (d) Raman spectra for pure  $\beta$ -Ga<sub>2</sub>O<sub>3</sub>, mixed GaO/GaZnO and pure spinel ZnGa<sub>2</sub>O<sub>4</sub>. Although observed XRD family of Bragg reflections of monoclinic and spinel-cubic are compatible, the different symmetry of the lattices resulted in very distinct Raman vibration modes with the main being A<sub>g</sub> and (T<sub>2g</sub>, A<sub>1g</sub>) for  $\beta$ -Ga<sub>2</sub>O<sub>3</sub> and ZnGa<sub>2</sub>O<sub>4</sub>, respectively.

The phase purity and crystallinity of the films was first analyzed by X-ray diffraction. **Figure 1-a** shows the XRD spectrum for the pure monoclinic  $\beta$ -Ga<sub>2</sub>O<sub>3</sub> (Zn-0) and Ga-Zn-O thin films with various Zn-flux ratios. The XRD patterns corroborate that  $\beta$ -Ga<sub>2</sub>O<sub>3</sub> was epitaxially grown following the monoclinic  $\beta$ -Ga<sub>2</sub>O<sub>3</sub> {-2m0m} plane family. The pure  $\beta$ -Ga<sub>2</sub>O<sub>3</sub> (GaO) exhibited the presence of 5 peaks at 18.91°, 38.32°, 58.99°, 82.09° and 110.29° corresponding to the (-201), (-402), (-603), (-804) and (-10 0 5) crystalline plans of the monoclinic  $\beta$ -Ga<sub>2</sub>O<sub>3</sub> which are indexed in the card PDF-00-041-1103. The X-ray diffractograms of the Ga-Zn-O samples show how they transitioned from a mixed solution of Ga<sub>2</sub>O<sub>3</sub> and ZnGa<sub>2</sub>O<sub>4</sub> phases (termed GaO/GaZnO) to a pure spinel ZnGa<sub>2</sub>O<sub>4</sub> phase. A double peak feature becomes obvious for the smallest Zn-fluxes, while larger Zn-fluxes samples (Zn-flux > 7  $\mu$ mol/min) only exhibited the shifted peak characteristic of the spinel {111} plane family reflections (**Figure 1-b**). As the Zn-flux increases, the pure  $\beta$ -Ga<sub>2</sub>O<sub>3</sub> reflections gradually vanish while, at the same time, a new spinel reflection (shifted to lower 2 $\theta$  values) appears. This new reflection appears at 18.47°, 37.40°, 57.50°, 79.70° and 106.42° corresponding to the (111), (222), (333), (444) and (555) crystalline planes of the cubic spinel ZnGa<sub>2</sub>O<sub>4</sub>, conformed to PDF-00-038-1240 The monoclinic-to-spinel 2-theta shift is more pronounced for

the larger index planes (i.e., larger thetas angles) as expected from Bragg's Law. **Figure 1-c** shows the Bragg's distance as a function of Zn flux for the spinel  $Fd\bar{3}m$  (444) / monoclinic  $C2/m$  (-804) peak. The inter-plane  $d$ -spacing is almost constant for  $\beta$ -Ga<sub>2</sub>O<sub>3</sub> phases (either in pure or mixed phases), and only a small increment of  $\sim 0.01$  Å is observed with increasing Zn content for the GaZnO in the coexistence region (GaO/GaZnO). In complement to these Bragg reflections separation, electron energy loss spectroscopy (EELS) profiles at nano-scale supports a spinodal decomposition during the total growth (and cooling) process. For pure ZnGa<sub>2</sub>O<sub>4</sub> phases plane  $d$ -spacing becomes constant again. The corresponding cubic  $a$ -parameter is equal to 8.33 Å, very close to reference values of PDF-00-038-1240 and values reported by Galazka et al.<sup>[38]</sup>. Therefore, spinel  $Fd\bar{3}m$  (111) / monoclinic  $C2/m$  (-201) orientation are epitaxially compatible, as studied by Horng *et al.*<sup>[11]</sup> and very close interplane spacing (1.17-1.20 Å) perpendicular to growth direction. Owing to their different lattice symmetries, however, they show distinct vibrational modes under Raman excitation (**Figure 1 -d**). The primary ZnGa<sub>2</sub>O<sub>4</sub> cubic spinel vibrational modes detected are A<sub>1g</sub> (709.7 cm<sup>-1</sup>) and T<sub>2g</sub> modes (603.1 cm<sup>-1</sup>) while the main  $\beta$ -Ga<sub>2</sub>O<sub>3</sub> vibrational modes detected are related to A<sub>g</sub> (651.2 cm<sup>-1</sup>), in agreement with previous literature (e.g.<sup>[52]</sup>). The oxide's optical bandgaps were determined by optical transmittance and reflectance spectroscopy. The optical transparency of the double polished sapphire substrate allows the determination of the intrinsic optical characteristics of the Ga<sub>2</sub>O<sub>3</sub> and ZnGa<sub>2</sub>O<sub>4</sub> thin-films. The optical transmittance and reflectance of  $\beta$ -Ga<sub>2</sub>O<sub>3</sub> and ZnGa<sub>2</sub>O<sub>4</sub>, pure and mixed phases (GaO/GaZnO), were determined by transmission spectroscopy all the range from UV-C to short wavelength infrared. As seen in **Figure 2-a**,  $\beta$ -Ga<sub>2</sub>O<sub>3</sub>, ZnGa<sub>2</sub>O<sub>4</sub> and mixed GaO/GaZnO exhibited a transparency above 80% in all wavelength range from  $\sim 300$  nm to 2500 nm. All films have sharp absorption edges of  $\sim 250$  nm. The optical bandgaps were determined by means of a Tauc's plot to be in the range of 4.6-4.8 eV (as shown in **Figure 2-b**). The optical band gap

for the pure  $\beta$ -Ga<sub>2</sub>O<sub>3</sub> and the GaO/GaZnO mixed phase is around ~4.6 eV, while it is slightly larger 4.8 eV for the pure ZnGa<sub>2</sub>O<sub>4</sub> (**Figure 2-c**).

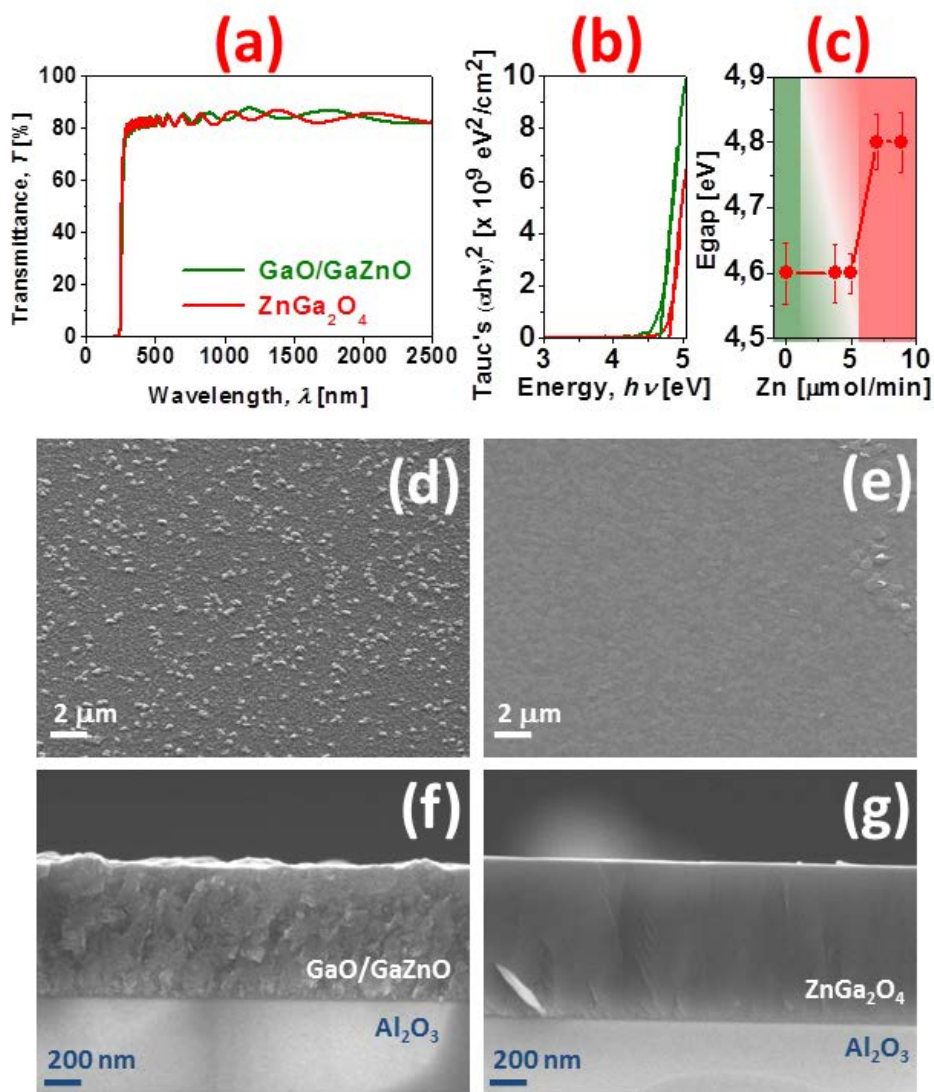


**Figure 2.** (a) Optical transmittance. (b) Tauc's plots (for the determination of the optical bandgap energy) for GaO/GaZnO mixed phase and for the pure ZnGa<sub>2</sub>O<sub>4</sub>. (c) Optical bandgap energy versus Zn-flux (μmol/min) used during the growth. (d) and (e) top view SEM images of the GaO/GaZnO mixed phase and the pure ZnGa<sub>2</sub>O<sub>4</sub>. (f) and (g) cross sectional SEM images of the GaO/GaZnO mixed phase and the pure ZnGa<sub>2</sub>O<sub>4</sub>.

The structural characteristics of the different composition of ternary oxides were further investigated by means of scanning electron microscope (SEM) and transmission electron microscope (TEM) equipped by energy-dispersive x-ray spectroscopy (EDS) and electron energy loss spectroscopy (EELS). Figure 2(d)-(g) presents a representative SEM top view and cross-sectional view of the ternary Ga-Zn-O having mixed phase GaO/GaZnO and pure spinel zinc gallate  $\text{ZnGa}_2\text{O}_4$ . It is already evidenced by SEM that a pure phase  $\text{ZnGa}_2\text{O}_4$  (Zn-9) exhibited a much planar morphology together with the absence of grains and grains boundaries as compared with a mixed GaO/GaZnO (Zn-4) sample.

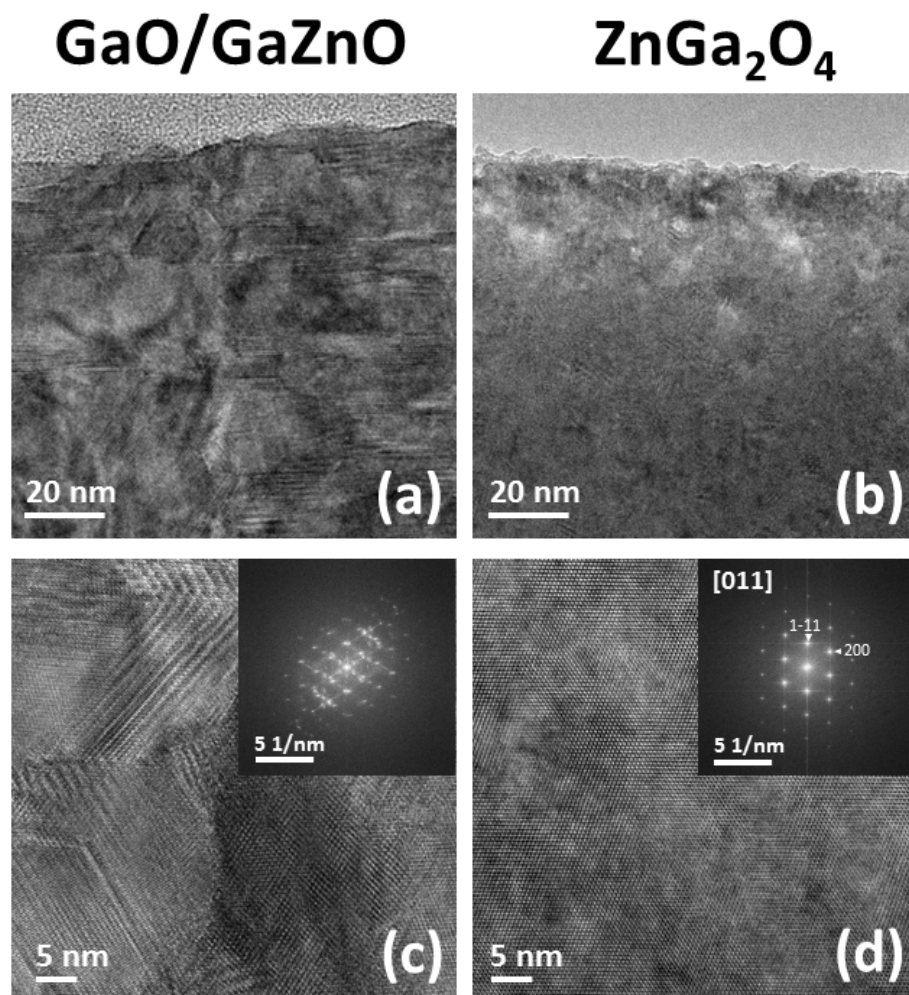


**Figure 3.** (a) Transmission electron microscope (TEM) images for (a) mixed phase GaO/GaZnO and (b) pure spinel  $\text{ZnGa}_2\text{O}_3$ . Higher resolution images are shown in (c) and in (d), for GaO/GaZnO and  $\text{ZnGa}_2\text{O}_3$ ,

respectively. The inset shows the fast Fourier transform of the images, with multiple reflections evidencing the phase mixture for the former and a perfectly oriented [011] view for  $\text{ZnGa}_2\text{O}_4$ .

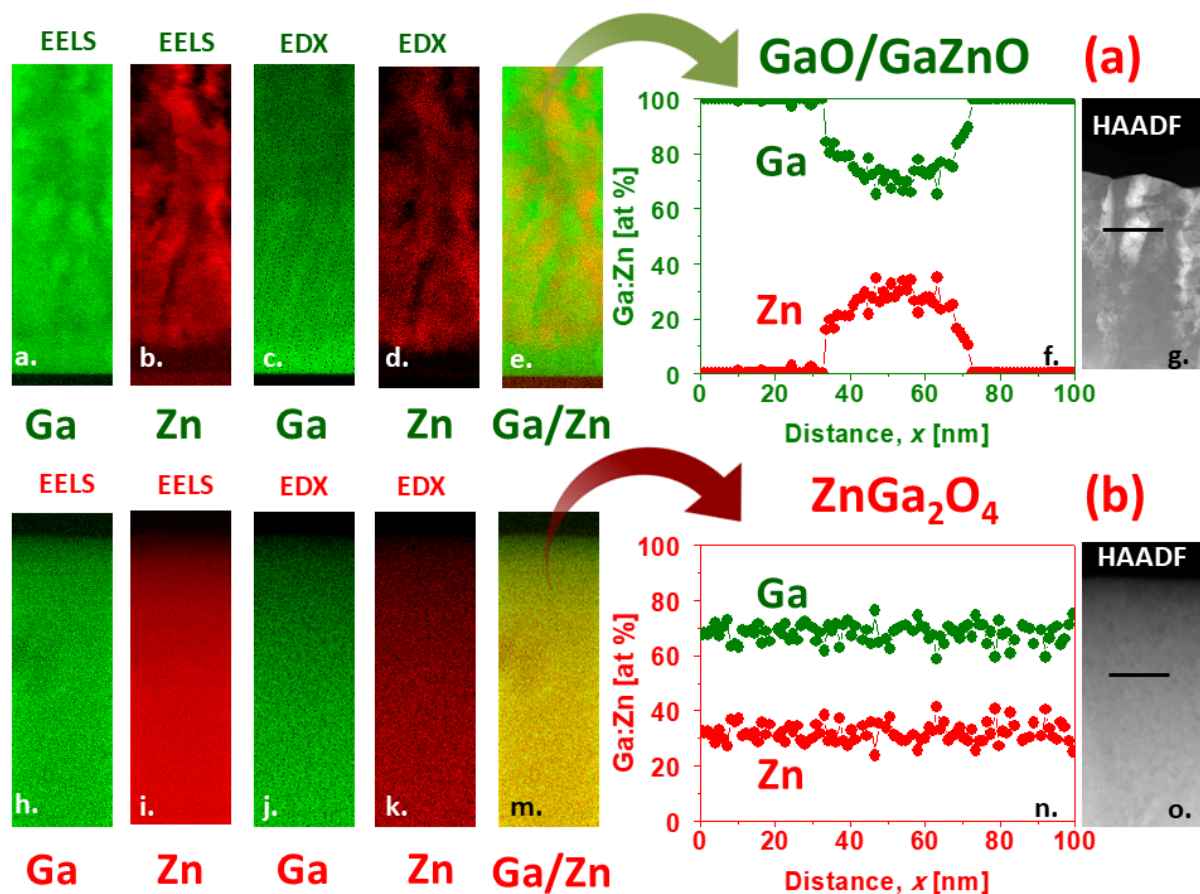


**Figure 4.** Cross-section STEM EELS Ga (a,h.), Zn (b.,i.), Ga/Zn (e.,m.) and EDX Ga (c.,j.), Zn (d.,k.) compositional maps and high-angle annular dark-field imaging (HAADF) STEM image (g.,o.) for (a) mixed phase GaO/GaZnO and (b) pure spinel  $\text{ZnGa}_2\text{O}_4$ . A compositional EDX profile is shown for the mixed and pure GaZnO showing its granular and homogeneous nature, respectively.

At higher resolution than the scanning electron microscopy, transmission electron microscopy (TEM) imaging corroborates the granular nature of the mixed GaO/GaZnO. In contrast,  $\text{ZnGa}_2\text{O}_4$  exhibited an epitaxial single crystal structure as shown in **Figure 3-a,-c** and in **Figure 3-b,-d**, for mixed GaO/GaZnO

and spinel  $\text{ZnGa}_2\text{O}_4$ , respectively. For the samples with the lowest Zn-fluxes, there is an intermix of pure GaO and GaZnO phases resulting in distorted grains of varying sizes of  $\sim 10\text{-}100$  nm in average and the corresponding large number of grain boundaries, coherent with a spinodal decomposition. In contrast, for Zn-fluxes above  $7 \mu\text{mol}/\text{min}$ , the Zn atoms are accommodated epitaxially within a single crystal spinel  $\text{ZnGa}_2\text{O}_4$  structure as shown in **Figure 3-c** and **3-d**. The Ga-Zn-O layers stoichiometry and atomic composition were further investigated by performing EELS and spectroscopy as shown in **Figure 4**. Corroborating the x-ray diffraction and Raman analysis, for the smallest Zn-fluxes (i.e., those that resulted in mixed GaO/GaZnO phases), the Zn EELS and EDX maps are non-homogeneous but Zn atoms are concentrated in  $\text{ZnGa}_2\text{O}_4$  grains within the  $\beta\text{-Ga}_2\text{O}_3$  matrix (**Figure 4-a**). It is worth noting that the EELS/EDX Zn concentration variations do not perfectly follow the high-angle annular dark-field imaging (HAADF) contrast variation in the STEM mode. This may be due to the fact that Zn (30) and Ga (31) have very similar atomic numbers. Pure spinel  $\text{ZnGa}_2\text{O}_4$  was found to be, in contrast, much more homogeneous in Zn and Ga compositions all over the layer. The stoichiometry of the Ga-Zn-O ternary oxide has been determined for a Zn-flux of  $8.9 \mu\text{mol}/\text{min}$  (Zn-9) to be 32% Zn and 68% Ga, and therefore, within the experimental error, it fits very well with a  $\text{ZnGa}_2\text{O}_4$  formulation.

An atomic fine chemical analysis of the surface was performed by x-ray photoelectron spectroscopy (XPS). XPS provides information about the Ga, Zn and O local bonding environment (not just element identification) either on pure  $\text{ZnGa}_2\text{O}_4$  or mixed GaO/GaZnO phases. The local atomic binding energies are affected by the cation formal oxidation state, the identity of its nearest-neighbor (Zn or Ga) atoms and its bonding hybridization. The two extreme compositions, monoclinic  $\beta\text{-Ga}_2\text{O}_3$  and wurtzite ZnO, grown in the same MOCVD chamber (see methods), were also included for comparison. **Figure 5** shows a detailed view of the main XPS peaks for (a) gallium ( $\text{Ga}2p$ ), (b) oxygen ( $\text{O}1s$ ), (c) zinc ( $\text{Zn}2p$ ) and (d)

carbon (C1s) at the surface of pure  $\beta$ -Ga<sub>2</sub>O<sub>3</sub> (GaO), pure wurtzite ZnO, mixed phase GaO/GaZnO (Zn-4) and pure spinel ZnGa<sub>2</sub>O<sub>4</sub>.

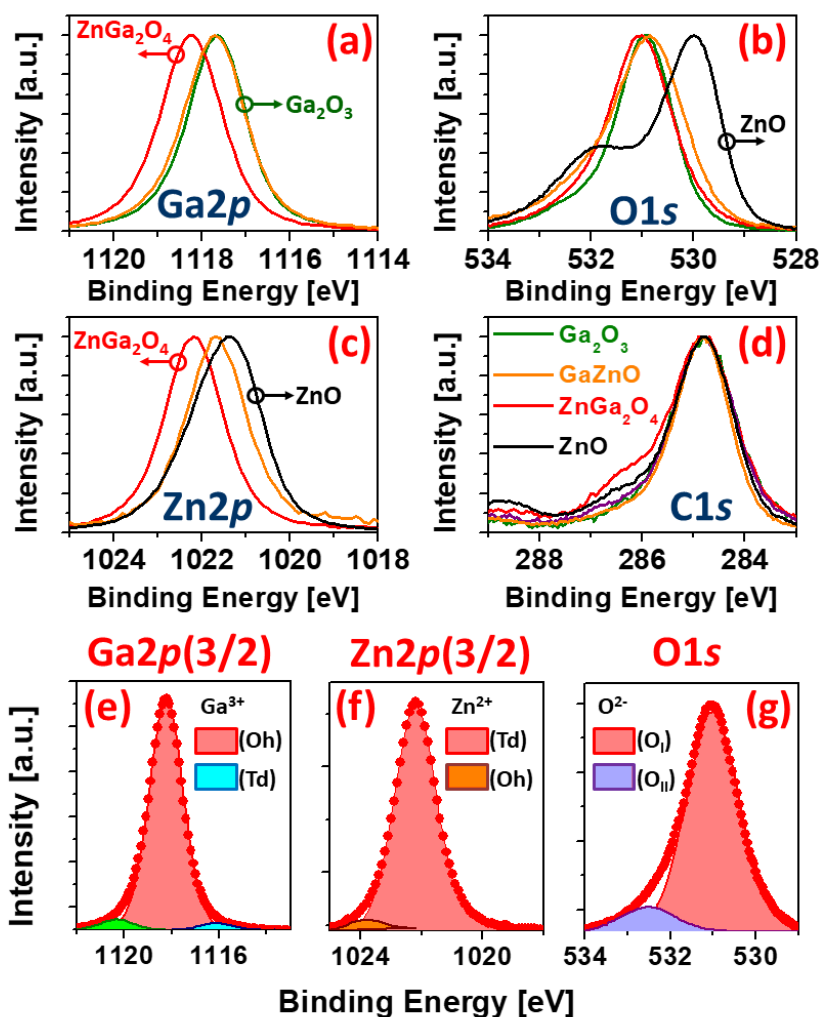


**Figure 5.** Detail (intensity normalized) of the main XPS peaks for (a) gallium (Ga2p - Ga2p<sub>3/2</sub>), (b) oxygen (O1s), (c) zinc (Zn2p - Zn2p<sub>3/2</sub>) and (d) adventitious carbon contamination (C1s, calibration for C-C bonds at 284.8 eV) at the surface of pure  $\beta$ -Ga<sub>2</sub>O<sub>3</sub> (GaO) with Zn-flux = 0  $\mu$ mol/min), mixed phase GaO/GaZnO (Zn-4), pure ZnGa<sub>2</sub>O<sub>4</sub> and a pure ZnO (wurtzite) reference (grown in the same chamber). Deconvolution of the main contributions of the (e) Ga2p<sub>3/2</sub>, (f) Zn2p<sub>3/2</sub> and (g) O1s oxygen peak for spinel ZnGa<sub>2</sub>O<sub>4</sub>.

Adventitious carbon contamination was used as a charge reference for XPS spectrum (by setting C1s maxima to a binding energy of 284.8 eV), which is a very common practice (**Figure 5-d**). Regarding O1s, a notable feature is the binding energy difference of the metal oxide oxygen peak in ZnO (~530 eV) (e.g.<sup>[53]</sup>) and the metal oxide oxygen peak binding energy (~531 eV) in monoclinic  $\beta$ -Ga<sub>2</sub>O<sub>3</sub> (e.g.<sup>[54,55]</sup>), GaO/GaZnO and spinel ZnGa<sub>2</sub>O<sub>4</sub>. According to Biesinger *et al.*<sup>[56]</sup>, the ZnO(II) O1s lattice oxide peak (O<sub>I</sub>) appears at 529.76 eV while the hydroxide, hydrated or defective oxygen (e.g. oxygen vacancies) shoulder (O<sub>II</sub>) in the O1s peak of ZnO appears shifted 1.49 eV, at 531.25 eV. In our case, the ZnO's lattice peak appears at 529,99 eV and the shoulder maxima appears at 531.69 eV which also presents the broad shape typical of multi-component contributions (i.e., -OH, H<sub>2</sub>O and V<sub>O</sub>). The  $\beta$ -Ga<sub>2</sub>O<sub>3</sub> (Zn-0) peak appears at 530,94 eV exhibiting a much less pronounced shoulder (see Fig. 5(g)). There also is no appreciable shoulder in GaO/GaZnO and spinel ZnGa<sub>2</sub>O<sub>4</sub>. The absence of shoulder features in O1s may be correlated with a lower donor compensation (very low concentration of oxygen vacancies). This correlates with the intrinsic *p*-type nature of the  $\beta$ -Ga<sub>2</sub>O<sub>3</sub>, GaO/GaZnO and ZnGa<sub>2</sub>O<sub>4</sub> layers, as it will be shown below by Hall transport measurements. For the reference spinel ZnGa<sub>2</sub>O<sub>4</sub> (Zn-9) the O1s lattice oxide peak appears at 530.99 eV while the Zn2*p*<sub>3/2</sub> and Ga2*p*<sub>3/2</sub> peak appears at 1022.20 eV and 1118.20 eV, respectively. The XPS quantification for the reference ZnGa<sub>2</sub>O<sub>4</sub> gives a stoichiometry of 30.4% Zn and 69.6% Ga, which is in close agreement with the quantification from TEM/EDX and the spinel stoichiometry.

As shown in **Figures 5-a and 5-c**, there is a significant shift of the binding energy of the Zn<sup>2+</sup> and Ga<sup>3+</sup> cations towards larger (Ga-O and Zn-O) binding energies which usually is regarded as an indication of cation oxidation (loss of electrons or an increase in the oxidation state). According to the first-principles calculations based on the density functional theory of Chao *et al.*<sup>[57]</sup>, with the introduction of the Zn impurity (Ga substitutional), the Zn atom loses almost all valence electrons (since the Zn electronegativity



is lower than Ga and the  $Zn^{2+}$  valence electrons are less than  $Ga^{3+}$ ) which may explain the  $Zn2p$  shift towards larger binding energies with increasing Zn-flux. The  $Zn2p_{3/2}$  peak for pure ZnO appears at 1021.34 eV while the  $Zn2p$  shifts to 1021.68 eV for the mixed GaO/GaZnO and 1022.20 eV for pure  $ZnGa_2O_4$  (Zn-9). Normal  $AB_2X_4$  spinels have all A cations in the tetrahedral site and all B cations in the octahedral site. Therefore, in the case of zinc gallate  $ZnGa_2O_4$ , Zn atoms lie in Zn-tetrahedral sites ( $Zn^{2+}(Td)$ ) and Ga atoms occupy the Ga-octahedral sites ( $Ga^{3+}(Oh)$ ) or  $Zn^{2+}(Td)Ga_2^{3+}(Oh)O_4^{2-}$ . In contrast to simple binary oxides (such as pure  $\beta$ - $Ga_2O_3$ ), where dominant defects are vacancies ( $V_o$  as donor and  $V_{Ga}$  as acceptor) and interstitials, dominant defects in spinels are suggested to be antisites [18]. These antisites are donor ( $Ga_{Zn}$ ) [donor-like  $Ga^{3+}(Oh)$ -on-Td antisite defects] and acceptor ( $Zn_{Ga}$ ) [acceptor-like  $Zn^{2+}(Td)$ -on-Oh antisite defects]. Intrinsic  $p$ -type self-doping of spinels implies therefore a minimization of the electrical influence of donor-like  $Ga^{3+}$ -on-Td antisite defects while maximizing the electrical influence of acceptor-like  $Zn^{2+}$ -on-Oh antisite defects. It has been suggested that in order to achieve  $p$ -type dopability [18], the concentration of  $Zn^{2+}$ -on-Oh should be maximized either, (i) by inducing Zn-rich off-stoichiometry using non-equilibrium growth or (ii) by choosing an  $Zn^{2+}$  element that naturally prefers Oh-coordination. Regarding the Zn favorite coordination, it has been suggested that Zn prefers a tetrahedral coordination when substituting Ga in  $\beta$ - $Ga_2O_3$  [58]. The  $\beta$ - $Ga_2O_3$  belongs to space group  $C2/m$  with two-fold rotation axis  $b$ . There are two different Ga sites, denoted as Ga(1) and Ga(2), and three different O sites, denoted as O(1), O(2), and O(3). Ga atoms are surrounded by O atoms in either tetrahedral Ga(1) or octahedral Ga(2) coordination. Skachkov and Lambrecht recently published a computational study of the electron paramagnetic resonance  $g$ -tensors of Zn-doped  $Ga_2O_3$  [58] where they determined that Zn would prefer the tetrahedral Ga(1) substitutional site, (Zn in ZnO has a tetrahedral bonding indeed as it has in normal  $ZnGa_2O_4$ ).

The cation distribution can be characterized by the inversion parameter  $y$ , which is defined as 2 times the fraction of  $Zn^{2+}$  ions in the octahedral sites. The degree of inversion in zinc gallate has been reported to be potentially estimated by the deconvolution of the  $Ga2p$  and  $Zn2p$  XPS peaks in two components at different binding energies (BEs) [59]. A  $Ga2p_{3/2}$  normal  $Ga^{3+}(Oh)$  contribution peaks at high BEs (1118.3 eV) and an *inversion*  $Ga^{3+}(Td)$  contribution is at significantly lower BEs (1116.8 eV). Analogously, a  $Zn2p_{3/2}$  normal  $Zn^{2+}(Td)$  is at lower BEs (~1022 eV) and an *inversion*  $Zn^{2+}(Oh)$  is at higher BEs (~1023 eV). Therefore, the tail contribution at larger binding energies in  $Zn2p_{3/2}$  would directly be a measure of  $Zn_{Ga}$ . In our case, the  $Ga2p_{3/2}$  peak appears precisely at 1118.2 eV and there is a small contribution shifted ~2 eV at lower BE (**Figure 5-e**) of ~2.8% the total area, while there would be around ~5.3% of  $Zn_{Ga}$  sites when the  $Zn2p_{3/2}$  peak is deconvoluted (Fig. 5(f)). An additional contribution may be observed for even larger BE in the  $ZnGa_2O_4$   $Ga2p_{3/2}$  peak (1120.1 eV) which, as far as we know, has not been discussed in previous literature yet.

## 2. $ZnGa_2O_4$ spinel electrical transport properties: An intrinsic $p$ -type semiconductor

For studying the actual electrical properties of the spinel zinc gallate layers, the  $ZnGa_2O_4$  thin-films resistivities and their corresponding Hall Effect were measured at high temperatures (450-850 K) in a Van Der Pauw configuration. Four electrical contacts by silver paint were made on each corner of a square shape (1x1 cm<sup>2</sup>) samples. As shown in **Figure 6-a**, a linear, non-rectifying current-voltage (I-V) behavior has been first corroborated at different temperatures, thus evidencing the Ohmic characteristic of the contacts. The resistivity vs temperature for spinel  $ZnGa_2O_4$  samples is shown in **Figure 6-b**.

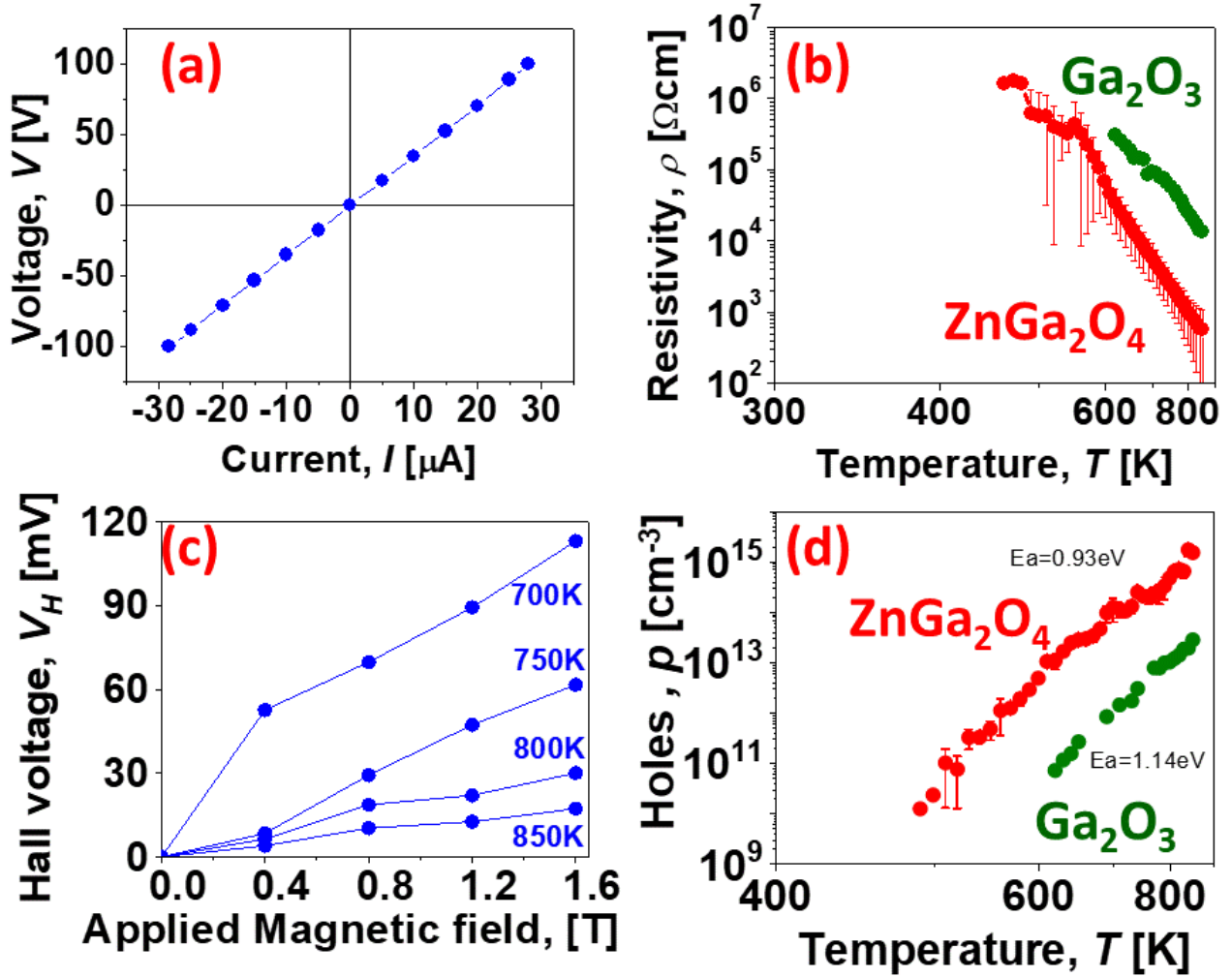


**Figure 6.** (a) Typical spinel ZnGa<sub>2</sub>O<sub>4</sub> Ohmic I-V characteristic at 850K. (b) Resistivity versus temperature for averaged (error bars) *p*-type spinel ZnGa<sub>2</sub>O<sub>4</sub> and the reference *p*-type β-Ga<sub>2</sub>O<sub>3</sub>. (c) Hall voltage ( $V_H$ ) versus magnetic field at different temperatures for a typical spinel ZnGa<sub>2</sub>O<sub>4</sub> sample. The Hall voltage slope is positive thus an indication of *p*-type conductivity. (d) Temperature dependence for Hall free hole concentration ( $p$  [cm<sup>-3</sup>]) for pure monoclinic reference β-Ga<sub>2</sub>O<sub>3</sub> and spinel ZnGa<sub>2</sub>O<sub>4</sub> films. An activation energy of the acceptor center ( $E_a$ ) was determined from the log ( $p$ ) vs  $1/T$  plot (Arrhenius) to be  $1.2 \pm 0.5$  eV and  $1.0 \pm 0.5$  eV for reference β-Ga<sub>2</sub>O<sub>3</sub> and spinel ZnGa<sub>2</sub>O<sub>4</sub> films, respectively.

The determination of the majority carrier type is, in practice, challenging when the sample is of high resistance ( $> 10^7 \Omega$ ) due to the difficulty in correctly extracting the Hall voltage ( $V_H$ ) from the total measured voltage. Elevating the temperature of measurement in our high temperature high impedance home-built Hall set-up enables measuring up to  $1\text{G}\Omega$  ( $10^9\Omega$ ) resistance sample. In a non-magnetic material,  $V_H$  is linearly proportional to the applied magnetic field and a positive sign slope for  $V_H(H)$  indicates that the majority charge carriers are  $p$ -type (holes). To further validate the sign of majority carriers, the Hall voltage dependence on the applied magnetic field was measured at different elevated temperatures and varying magnetic fields from 0 to 1.6 T. As shown in **Figure 6-c**, the positive  $V_H$  *linearly* increases with perpendicularly applied magnetic field. This confirms that the layer was  $p$ -type. The temperature dependence for Hall hole concentration is shown in **Figure 7-d**.  $\text{ZnGa}_2\text{O}_4$   $p$ -type films and, at the highest available temperature of 850 K, the free hole concentration was measured to be as large as  $p = 2 \times 10^{15} \text{ cm}^{-3}$ , while for pure  $\beta\text{-Ga}_2\text{O}_3$  the hole concentration was 100 times smaller (i.e.,  $p = 1.4 \times 10^{13} \text{ cm}^{-3}$ ). From the  $\log(p)$  vs  $1/T$  plot, the activation energy ( $E_a$ ) of the acceptor centers have been determined to be  $1.2 \pm 0.5$  eV and  $1.0 \pm 0.5$  eV.

As mentioned before, according to previous literature <sup>[42–46]</sup>, the most plausible origin of  $p$ -type conductivity in ternary spinel  $\text{ZnGa}_2\text{O}_4$  would be the anti-site  $\text{Zn}_{\text{Ga}}$  center, in contrast to normal binary oxides where it is generally ascribed to a cation vacancy or interstitial. In our case, undoped  $\beta\text{-Ga}_2\text{O}_3$  and spinel  $\text{ZnGa}_2\text{O}_4$  exhibit similar value of acceptor center activation energies ( $E_a$ ) but still 100 times more free holes in  $\text{ZnGa}_2\text{O}_4$  films. A canonical interpretation of our Hall Effect measurements would suggest that the point defect responsible for  $p$ -type conductivity would be *the same* (or at least to lie in a similar energetic position within the bandgap) in both materials, while the differences in  $p$  [ $\text{cm}^{-3}$ ] (free hole

concentration) would be related to a different compensation ratio. The compensation by donor defects, in another word  $N_D/N_A$  ratio, would be smaller in  $ZnGa_2O_4$  films than in pure  $\beta-Ga_2O_3$ , grown with the same parameters (i.e., oxygen partial pressure and temperature). The increase of acceptors,  $N_A$  might be explained with creation of anti-site  $Zn_{Ga}$  acceptor defects in  $ZnGa_2O_4$  spinel. This defect being deep cannot play an “effective” acceptor role with small ionization energy, but acts as a compensator-donor killer, thus resulting enhancement of hole concentrations. Experimental Hall hole mobilities for spinel  $ZnGa_2O_4$  were found to be in the range of  $\mu = 7 - 10 \text{ cm}^2/Vs$  (680-850 K). Such a remarkable high value of acceptor mobilities for *p*-type TCO confirms that conductivity is by band activation mechanism and not by small polaron as it often has been reported to be the case in other spinels<sup>[47]</sup>. That is a very important feature for *p*-type ternary  $ZnGa_2O_4$  oxide, since having delocalized holes in undoped state, gives strong promises of efficient doping capability for increasing free carriers.

### 3. The $ZnGa_2O_4$ Valence Band: Experiment vs ab-initio simulations

Once the  $ZnGa_2O_4$  layers *p*-type conductivity has been determined by high-temperature Hall Effect, the nature of the oxide’s semiconductor valence band has been further investigated by means of high-resolution X-ray photoelectron spectroscopy and ab-initio calculations. XPS also is an excellent chemical method to investigate a material’s valence band characteristics and brings additional evidence of the presence of states within the bandgap<sup>[60–62]</sup>. When used in high resolution in the valence band vicinity (i.e., for the lowest binding energies), it is possible to directly detect whether there are states in the lower part (i.e., smaller than the intrinsic energy level or ~mid-gap) of the bandgap (those responsible for *p*-type character)<sup>[63]</sup>.

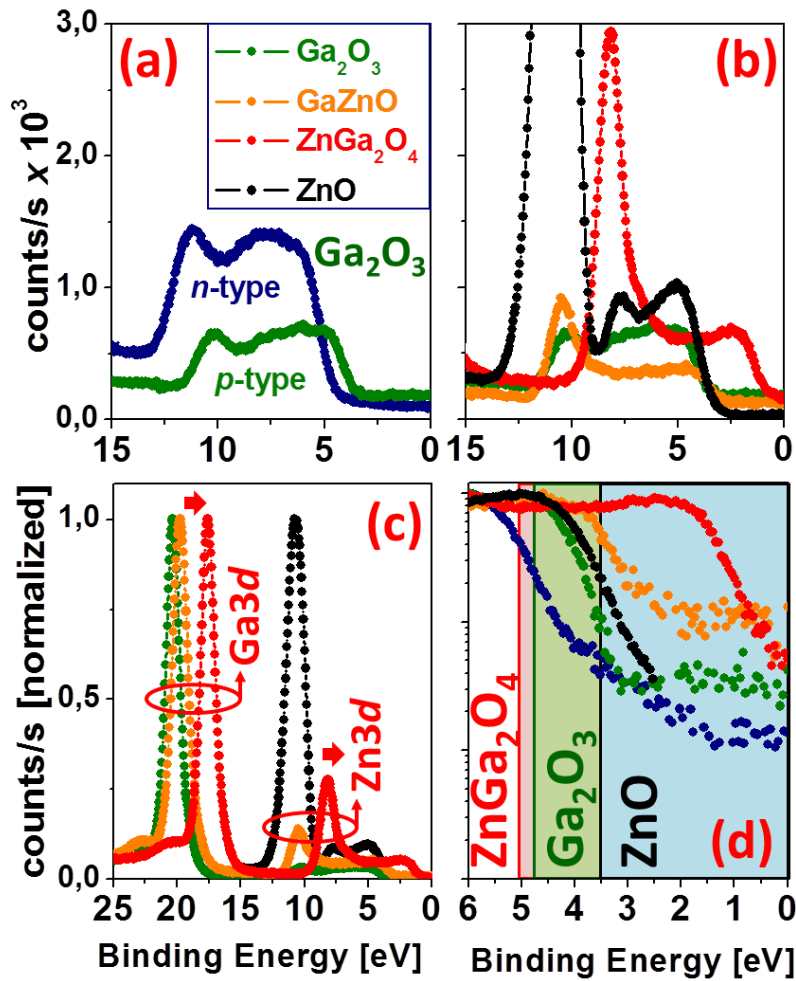


**Figure 7.** (a) Experimental XPS high-resolution valence band for the *p*-type  $\beta$ -Ga<sub>2</sub>O<sub>3</sub> and a reference *n*-type  $\beta$ -Ga<sub>2</sub>O<sub>3</sub>. (b) Experimental XPS high-resolution of the first valence band group for pure *p*-type  $\beta$ -Ga<sub>2</sub>O<sub>3</sub>, *p*-type mixed phases of Ga<sub>2</sub>O<sub>3</sub>/ZnGa<sub>2</sub>O<sub>4</sub> (GaZnO) and *p*-type pure spinel ZnGa<sub>2</sub>O<sub>4</sub>. An undoped ZnO specimen is included for comparison. The valence band maxima (VBM) is from O2*p* states for all the samples but those compounds containing zinc atoms exhibit an important additional contribution of Zn3*d* states (c) *Idem*, for the first and the second group of valence bands. The second group of bands is contributed primarily by Ga3*d* (in the compounds containing Gallium) and O1*s*. (d) A zoom of the valence band region (VBM) showing the presence of tail states in the lower part of the bandgap for the *p*-type compounds (the value of the bandgap is depicted for ZnO,  $\beta$ -Ga<sub>2</sub>O<sub>3</sub> and ZnGa<sub>2</sub>O<sub>4</sub>).

Our starting point was pure monoclinic *p*-type  $\beta$ -Ga<sub>2</sub>O<sub>3</sub> (Zn-0). As shown in **Figure 7-a**, when  $\beta$ -Ga<sub>2</sub>O<sub>3</sub> was grown in strong compensation conditions at high oxygen flux, the layers were found to be highly resistive *p* type in nature. When compared with a reference (Si-doped) *n*-type  $\beta$ -Ga<sub>2</sub>O<sub>3</sub> single crystal, they exhibited a shift towards smaller binding energies and a number of tail states arise at ~1.5-1.0 eV from the conduction band edge (**Figure 7-d**). The *n*-type control sample is a commercial (Novel Crystal Technology, Inc.) nominally *n*-type Si-doped  $\beta$ -Ga<sub>2</sub>O<sub>3</sub> ( $N_D-N_A = 1.3 \times 10^{18} \text{ cm}^{-3}$ ) epitaxy (500 nm) grown on a single crystal  $\beta$ -Ga<sub>2</sub>O<sub>3</sub> (labelled “*n*-type”). For our samples, the valence band edge is shifted towards more *p*-type using the adventitious C-C 284.8 eV as the calibration peak (lower Fermi level implies more *p*-type character). **Figures 7b)** and **7-c** show the experimental valence region for *p*-type  $\beta$ -Ga<sub>2</sub>O<sub>3</sub>, *p*-type mixed phases of Ga<sub>2</sub>O<sub>3</sub>/ZnGa<sub>2</sub>O<sub>4</sub> (GaZnO) and *p*-type pure spinel ZnGa<sub>2</sub>O<sub>4</sub>. These samples were defined by increasing progressively the Zn-flux within the MOCVD chamber. The other stoichiometric end, an undoped ZnO specimen, is included for comparison (i.e. Ga-flux 0  $\mu\text{mol/min}$ ). Indeed, the spinel ternary ZnGa<sub>2</sub>O<sub>4</sub>, in terms of composition, can be regarded as a metastable alloy of Ga<sub>2</sub>O<sub>3</sub> and ZnO binary oxides in a cubic  $Fd\bar{3}m$  arrangement, where Zn and Ga atoms have tetrahedral (T<sub>d</sub>) and octahedral (O<sub>h</sub>) coordination bounds with oxygen, respectively. While  $\beta$ -Ga<sub>2</sub>O<sub>3</sub> have Ga-O (T<sub>d</sub>) and (O<sub>h</sub>) bounds (1:1), wurtzite ZnO presents only T<sub>d</sub> Zn-O bounds. **Figure 7-d** is a zoom of the valence band region (VBM) showing the presence of tail states in the lower part of the bandgap for the *p*-type compounds (the value of the bandgap is depicted for ZnO,  $\beta$ -Ga<sub>2</sub>O<sub>3</sub> and ZnGa<sub>2</sub>O<sub>4</sub>. For reference ZnO, the Fermi level (as measured from the valence band maxima or VBM) lies in the mid-gap but in the upper-half of the bandgap (~2.50 eV), an indication of their native highly resistive but *n*-type character. In contrast, the ZnGa<sub>2</sub>O<sub>4</sub> spinel exhibit an smaller Fermi level energy (~0.5 eV) and thus, the acceptor states would lie within the bandgap closer to the valence band maximum than in *p*-type  $\beta$ -Ga<sub>2</sub>O<sub>3</sub>, an observation that is coherent with

the experimental higher free hole concentrations by Hall Effect in spinel ZnGa<sub>2</sub>O<sub>4</sub>. In agreement with this fact, it may be observed that, even for the mixed phase of  $\beta$ -Ga<sub>2</sub>O<sub>3</sub> and spinel ZnGa<sub>2</sub>O<sub>4</sub>, the acceptor tail states are significantly shifted towards the valence band (label “GaZnO” in **Figure 7**).

Ab-initio simulation (see methods) are used to compare (vs experiment) the oxide’s theoretical bandgap energies and to identify the main components of the experimental XPS valence bands in **Figures 7(-c and 7-d)**. The calculated bandgap energies ( $E_g$ ) and the semiconductor band structure in the vicinity of VBM are shown in **Figure 8**. The theoretical direct band gaps are 4.73 eV, 3.40 eV and 5.06 eV, for monoclinic  $\beta$ -Ga<sub>2</sub>O<sub>3</sub>, wurtzite ZnO and spinel ZnGa<sub>2</sub>O<sub>4</sub>, respectively. These  $E_g$  values are in agreement with the values extracted for the optical bandgap measured by optical spectroscopy (see section 2). Further simulation details are given in the method section.

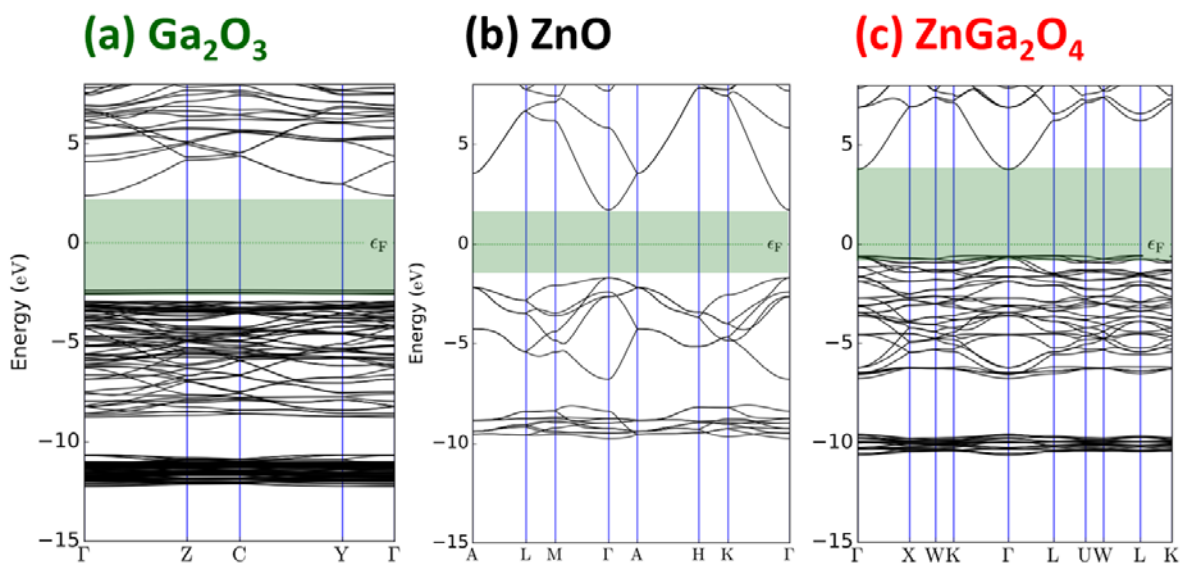


**Figure 8.** Calculated bandgap energy for (a) monoclinic  $\beta$ -Ga<sub>2</sub>O<sub>3</sub>, (b) wurtzite ZnO and (c) spinel ZnGa<sub>2</sub>O<sub>4</sub> by using DFT.



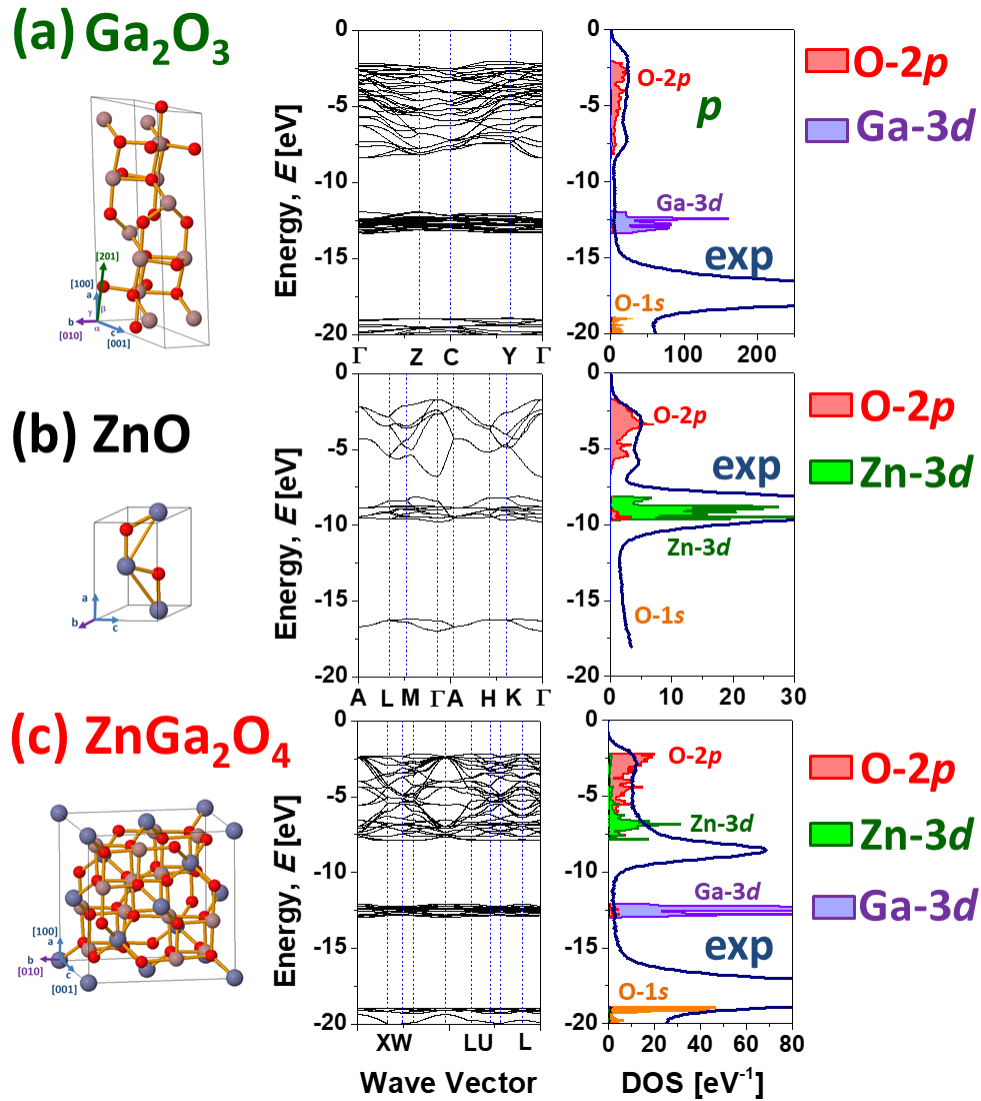


**Figure 9.** Determination of the valence bands main atomic contribution and their density of states (DOS) for (a) monoclinic  $\beta$ - $\text{Ga}_2\text{O}_3$ , (b) wurtzite  $\text{ZnO}$  and (c) spinel  $\text{ZnGa}_2\text{O}_4$  by using DFT.

A closer look of the theoretical valence band electronic structure and its electronic configuration is shown in **Figure 9**. The valence band maxima (VBM) is from  $\text{O}2p$  states for all the oxides under study but those compounds containing zinc atoms and gallium atoms exhibit further contributions of  $\text{Zn}3d$  states ( $\text{ZnO}$ ) and  $\text{Ga}3d$  states ( $\text{Ga}_2\text{O}_3$ ), respectively (**Figures 9-a** and **9-b**). In the case of the spinel  $\text{ZnGa}_2\text{O}_4$ , there are three main features observed in the experimental which are ascribed to  $\text{O}2p$ ,  $\text{Zn}3d$  and  $\text{Ga}3d$  respectively

as shown in **Figure 7-c**. When calibrated with respect adventitious C-C (284.8 eV), it is noticeable the shift observed for the  $Zn3d$  and  $Ga3d$  towards smaller binding energies for the ternary spinel  $ZnGa_2O_4$  oxide. The  $Ga3d$  peak appears at 20.73 eV, 19.75 eV and 17.60 eV, for  $\beta$ - $Ga_2O_3$ , mixed phases and spinel  $ZnGa_2O_4$ , respectively. For the  $Zn3d$  contribution, the peak values are 10.79 eV, 10.40 eV and 8.05 eV, for ZnO, mixed phases and spinel  $ZnGa_2O_4$ , respectively. This decrease in the first valence band binding energies is coherent with the smaller Fermi level energy derived for spinel  $ZnGa_2O_4$  ( $\sim 0.5$  eV). As shown in **Figure 9-b**, the GGA+U approximation reproduces well the valence band experimental features for our ZnO. Semi-empirical approach (LDA-1/2) and Meta\_GGA (one of semi-local approximations functionals as an alternative of the DFT-1/2) were used for spinel  $ZnGa_2O_4$  and  $\beta$ - $Ga_2O_3$ , respectively. Although, the binding energies for the  $Ga3d$  states are particularly underestimated in gallium oxide related compounds (we are using for the sake of simplicity local or semilocal exchange correlation), the simulation procedure still reproduces the main valence band experimental peak contributions and ordering <sup>[64]</sup>. The BE divergences would be related to the fact that, in monoclinic  $\beta$ - $Ga_2O_3$  and spinel  $ZnGa_2O_4$ , shallow  $Ga3d$  core electrons have to be treated as valence electrons (for example, by using many-body perturbation theory within Hedin's GW approach) <sup>[65]</sup>.

As demonstrated for  $\beta$ - $Ga_2O_3$  <sup>[49]</sup>, the Kroger's thermodynamic analysis predicted that high oxygen pressures guarantee the appearance of uncompensated hole conductivity effectively suppressing the compensation by native donors, which are associated primarily to oxygen vacancies ( $V_O$ ). As opposed to ZnO, thanks to the  $\beta$ - $Ga_2O_3$  particular point defect chemistry and the large formation energy of oxygen vacancies <sup>[66]</sup> (the native donor which can play the role of compensators for holes), it is possible to achieve the realization of stable  $p$ -type conductivity even in undoped layers. Indeed, as mentioned before, the ZnO layer presents a much larger Fermi energy level of  $\sim 2.5$  eV which suggest a natural  $n$ -type character (in

line with *n*-type (Si-doped) reference  $\beta$ -Ga<sub>2</sub>O<sub>3</sub>) and contrary to the rest of the *p*-type layers grown. As shown in **Figure 7-d**-, the entire valence band is further shifted towards smaller Fermi levels for the spinel ZnGa<sub>2</sub>O<sub>4</sub> when compared to the starting *p*-type  $\beta$ -Ga<sub>2</sub>O<sub>3</sub> and mixed GaZnO phases. It is worth noticing that the C1s calibration shift is believed to have no effect in the determination of the ZnGa<sub>2</sub>O<sub>4</sub> valence band (i.e. Fermi level, Ga3*d* or Zn3*d* energies - see methods).

This enhanced *p*-type dopability may be ascribed to the natural spinel tendency to a certain degree of inversion and the corresponding creation of acceptor antisites (Zn<sub>Ga</sub>). In this sense, preliminary DFT simulations for the ZGO antisite pair were conducted (see methods). A 112-atom supercell was built (Zn<sub>16</sub>Ga<sub>32</sub>O<sub>64</sub>) and the simulated band structure and DOS shown the creation of two acceptor energy levels, which is consistent with what was already reported by De Vos *et al.* [46]. These two energy states are contributed by the electrons in Zn-3*d* and O-2*p* orbitals. The antisite induced acceptor energy states mainly attributed to Zn<sub>Ga</sub> is therefore a strong candidate for explaining the origin of measured *p*-type conductivity. Here, the *p*-type spinel character has been achieved by tuning our growth methodology by defining highly compensated  $\beta$ -Ga<sub>2</sub>O<sub>3</sub> in high oxygen pressure (to remove the remote donor) and then, adding the Zn-atoms at high Zn-flux. As the gallium vacancy is the most plausible acceptor in our  $\beta$ -Ga<sub>2</sub>O<sub>3</sub> layers, the Zn-atoms will incorporate naturally in some T<sub>d</sub> and O<sub>h</sub> sites and play role of donor killer, promoting native hole conductivity of our spinel ZnGa<sub>2</sub>O<sub>4</sub>.

#### 4. Conclusions

To exploit the full potential of any emerging ultra-wide bandgap (UWBG) solid-state semiconductor technology, a good control (over several orders of magnitude) of the *n*-type and *p*-type conductivity should be attained. Although spinel's dopability was already theoretically predicted, no *p*-type conductivity has

been corroborated for UWBG ZnGa<sub>2</sub>O<sub>4</sub> spinel's yet. To achieve efficient *p*-type doping in wide band gap materials, the first step is the realization of native hole conductivity in the undoped state. Following this approach, it is further demonstrated in this work that the ternary ultra-wide band gap (~5 eV) spinel zinc gallate (ZnGa<sub>2</sub>O<sub>4</sub>) is the native *p*-type ternary oxide semiconductor with the widest bandgap. This achievement opens-up an important perspective for successful UWBG *p*-type doping, thus paving the way to bipolar extreme *spinel electronics* for a range of emerging energy applications (e.g. opto and power electronics). Furthermore, as a new acceptor member of the emerging gallium oxide family technology, this spinel ZnGa<sub>2</sub>O<sub>4</sub> phase, (stabilized after Zn incorporation), is structurally compatible with the monoclinic and more stable  $\beta$ -Ga<sub>2</sub>O<sub>3</sub> phase where suitable growth directions are [111] and [-201] for ZnGa<sub>2</sub>O<sub>4</sub> and  $\beta$ -Ga<sub>2</sub>O<sub>3</sub>, respectively.

## **Acknowledgements**

Hagar Mohammed would like to acknowledge Cultural Affairs and Massion Sector, Egyptian Ministry for Higher Education for her fellowship giving possibility work in France. EdC acknowledges Spanish MINECO Juan de la Cierva Fellowship JC-2015-25201. APT acknowledges Agencia Estatal de Investigación (AEI) and Fondo Europeo de Desarrollo Regional (FEDER) under contract ENE2015-74275-JIN. The ICN2 is funded by the CERCA programme / Generalitat de Catalunya and by the Severo Ochoa programme of the Spanish Ministry of Economy, Industry and Competitiveness (MINECO, grant no. SEV-2017-0706). We express our thanks to G.Bouchez for his assistance for optical measurements.

## References

- [1] Horng, Ray-Hua, Chiung-Yi Huang, Sin-Liang Ou, Tzu-Kuang Juang, and Po-Liang Liu, "Epitaxial Growth of  $ZnGa_2O_4$ : A New, Deep Ultraviolet Semiconductor Candidate" *Cryst. Growth Des.* **2017**, 17, 6071–78.
- [2] J. Y. Tsao, S. Chowdhury, M. A. Hollis, D. Jena, N. M. Johnson, K. A. Jones, R. J. Kaplar, S. Rajan, C. G. Van de Walle, E. Bellotti, C. L. Chua, R. Collazo, M. E. Coltrin, J. A. Cooper, K. R. Evans, S. Graham, T. A. Grotjohn, E. R. Heller, M. Higashiwaki, M. S. Islam, P. W. Juodawlkis, M. A. Khan, A. D. Koehler, J. H. Leach, U. K. Mishra, R. J. Nemanich, R. C. N. Pilawa-Podgurski, J. B. Shealy, Z. Sitar, M. J. Tadjer, A. F. Witulski, M. Wraback, J. A. Simmons, "Ultrawide-Bandgap Semiconductors: Research Opportunities and Challenges" *Adv. Electron. Mater.* **2018**, 4, 1600501.
- [3] L. Nagarajan, R. A. De Souza, D. Samuelis, I. Valov, A. Börger, J. Janek, K.-D. Becker, P. C. Schmidt, M. Martin, "A chemically driven insulator–metal transition in non-stoichiometric and amorphous gallium oxide" *Nat. Mater.* **2008**, 7, 391.
- [4] E. Chikoidze, D. J. Rogers, F. H. Teherani, C. Rubio, G. Sauthier, H. J. Von Bardeleben, T. Tchelidze, C. Ton-That, A. Fellous, P. Bove, E. V. Sandana, Y. Dumont, A. Perez-Tomas, "Puzzling robust 2D metallic conductivity in undoped  $\beta$ - $Ga_2O_3$  thin films" *Materials Today Physics* **2019**, 8, 10.
- [5] J. Kim, T. Sekiya, N. Miyokawa, N. Watanabe, K. Kimoto, K. Ide, Y. Toda, S. Ueda, N. Ohashi, H. Hiramatsu, H. Hosono, T. Kamiya, "Conversion of an ultra-wide bandgap amorphous oxide insulator to a semiconductor" *NPG Asia Materials* **2017**, 9, e359.
- [6] P. Gorai, R. W. McKinney, N. M. Haegel, A. Zakutayev, V. Stevanovic, "A computational survey of semiconductors for power electronics" *Energy Environ. Sci.* **2019**, 12, 3338; S. B. Reese, T. Remo, J. Green, A. Zakutayev, "How Much Will Gallium Oxide Power Electronics Cost?" *Joule* **2019**, 3, 903.

- [7] A. Pérez-Tomás, E. Chikoidze, M.R. Jennings, S.A.O. Russell, F.H. Teherani, P. Bove, E.V. Sandana, D.J. Rogers, "Wide and ultra-wide bandgap oxides: where paradigm-shift photovoltaics meets transparent power electronics" *Proc. SPIE 10533, Oxide-based Materials and Devices IX*, 105331Q (2018); <https://doi.org/10.1117/12.2302576>
- [8] S. J. Pearton, F. Ren, M. Tadjer, J. H. Kim, "Perspective:  $Ga_2O_3$  for ultra-high power rectifiers and MOSFETS" *J. Appl. Phys.* **2018**, 124, 220901.
- [9] M. Higashiwaki, G. H. Jessen, "The dawn of gallium oxide microelectronics" *Appl. Phys. Lett.* **2018**, 112, 060401.
- [10] A. Pérez-Tomás, E. Chikoidze, Y. Dumont, M. R. Jennings, S. O. Russell, P. Vales-Castro, G. Catalan, M. Lira-Cantú, C. Ton –That, F. H. Teherani, V. E. Sandana, P. Bove, D. J. Rogers, "Giant bulk photovoltaic effect in solar cell architectures with ultra-wide bandgap  $Ga_2O_3$  transparent conducting electrodes" *Mater. Today Energy.* **2019**, 14, 100350.
- [11] Y. S. Lee, D. Chua, R. E. Brandt, S. C. Siah, J. V. Li, J. P. Mailoa, S. W. Lee, R. G. Gordon, T. Buonassisi, "Atomic Layer Deposited Gallium Oxide Buffer Layer Enables 1.2 V Open-Circuit Voltage in Cuprous Oxide Solar Cells" *Adv. Mater.* **2014**, 26, 4704.
- [12] W.-Y. Kong, G.-A. Wu, K.-Y. Wang, T.-F. Zhang, Y.-F. Zou, D.-D. Wang, L.-B. Luo, "Graphene- $\beta$ - $Ga_2O_3$  Heterojunction for Highly Sensitive Deep UV Photodetector Application" *Adv. Mater.* **2016**, 28, 10725.
- [13] K. Ellmer, "Past achievements and future challenges in the development of optically transparent electrodes" *Nat. Photonics.* **2012**, 6, 809.
- [14] X. Yu, T. J. Marks, A. Facchetti, "Metal oxides for optoelectronic applications" *Nat. Mater.* **2016**, 15, 383.

- [15] A. Pérez-Tomás, "Functional Oxides for Photoneuromorphic Engineering: Toward a Solar Brain" *Adv. Mater. Interfaces*. **2019**, *0*, 1900471.
- [16] Z. Galazka, S. Ganschow, R. Schewski, K. Irmischer, D. Klimm, A. Kwasniewski, M. Pietsch, A. Fiedler, I. Schulze-Jonack, M. Albrecht, T. Schröder, M. Bickermann, "Ultra-wide bandgap, conductive, high mobility, and high quality melt-grown bulk  $ZnGa_2O_4$  single crystals" *APL Mater.* **2019**, *7*, 022512 [17] L.-C. Cheng, C.-Y. Huang, R.-H. Horng, "Thickness Effect on Operational Modes of  $ZnGa_2O_4$  MOSFETs" *IEEE J. Electron Devices Soc.* **2018**, *6*, 432.
- [18] M. Stoica, C. S Lo, "P-type zinc oxide spinels: application to transparent conductors and spintronics" *New J. Phys.* **2014**, *16*, 055011.
- [19] J. D. Perkins, T. R. Paudel, A. Zakutayev, P. F. Ndione, P. A. Parilla, D. L. Young, S. Lany, D. S. Ginley, A. Zunger, N. H. Perry, Y. Tang, M. Grayson, T. O. Mason, J. S. Bettinger, Y. Shi, M. F. Toney, "Inverse design approach to hole doping in ternary oxides: Enhancing p-type conductivity in cobalt oxide spinels" *Phys. Rev. B* 2011, *84*, 205207; A. Zakutayev, T. R. Paudel, P. F. Ndione, J. D. Perkins, S. Lany, A. Zunger, D. S. Ginley, "Cation off-stoichiometry leads to high p-type conductivity and enhanced transparency in  $Co_2ZnO_4$  and  $Co_2NiO_4$  thin films" *Phys. Rev. B* 2012, *85*, 085204.
- [20] Q. Zhao, Z. Yan, C. Chen, J. Chen, "Spinels: Controlled Preparation, Oxygen Reduction/Evolution Reaction Application, and Beyond" *Chem. Rev.* **2017**, *117*, 10121.
- [21] S. Chu, Y. Cui, N. Liu, "The path towards sustainable energy" *Nat. Mater.* **2016**, *16*, 16.
- [22] A. Kwade, W. Haselrieder, R. Leithoff, A. Modlinger, F. Dietrich, K. Droeder, "Current status and challenges for automotive battery production technologies" *Nat. Energy* **2018**, *3*, 290.

- [23] L. A.-W. Ellingsen, C. R. Hung, G. Majeau-Bettez, B. Singh, Z. Chen, M. S. Whittingham, A. H. Strømman, "Nanotechnology for environmentally sustainable electromobility" *Nat. Nanotechnol.* **2016**, *11*, 1039.
- [24] P. Canepa, S.-H. Bo, G. Sai Gautam, B. Key, W. D. Richards, T. Shi, Y. Tian, Y. Wang, J. Li, G. Ceder, "High magnesium mobility in ternary spinel chalcogenides" *Nat. Commun.* **2017**, *8*, 1759.
- [25] C. Wu, S. Gu, Q. Zhang, Y. Bai, M. Li, Y. Yuan, H. Wang, X. Liu, Y. Yuan, N. Zhu, F. Wu, H. Li, L. Gu, J. Lu, "Electrochemically activated spinel manganese oxide for rechargeable aqueous aluminum battery" *Nat. Commun.* **2019**, *10*, 73.
- [26] Y. Wang, Y. Yang, S. Jia, X. Wang, K. Lyu, Y. Peng, H. Zheng, X. Wei, H. Ren, L. Xiao, J. Wang, D. A. Muller, H. D. Abruña, B. J. Hwang, J. Lu, L. Zhuang, "Synergistic Mn-Co catalyst outperforms Pt on high-rate oxygen reduction for alkaline polymer electrolyte fuel cells" *Nat. Commun.* **2019**, *10*, 1506.
- [27] C. Zeng, T. Hu, N. Hou, S. Liu, W. Gao, R. Cong, T. Yang, "Photocatalytic pure water splitting activities for ZnGa<sub>2</sub>O<sub>4</sub> synthesized by various methods" *Mater. Res. Bull.* **2015**, *61*, 481.
- [29] M. Zhong, Y. Li, I. Yamada, J.-J. Delaunay, "ZnO–ZnGa<sub>2</sub>O<sub>4</sub> core–shell nanowire array for stable photoelectrochemical water splitting" *Nanoscale* **2012**, *4*, 1509.
- [28] W. Zhang, J. Zhang, Z. Chen, T. Wang, "Photocatalytic degradation of methylene blue by ZnGa<sub>2</sub>O<sub>4</sub> thin films" *Catal. Commun.* **2009**, *10*, 1781.
- [30] S. C. Yan, S. X. Ouyang, J. Gao, M. Yang, J. Y. Feng, X. X. Fan, L. J. Wan, Z. S. Li, J. H. Ye, Y. Zhou, Z. G. Zou, "A Room-Temperature Reactive-Template Route to Mesoporous ZnGa<sub>2</sub>O<sub>4</sub> with Improved Photocatalytic Activity in Reduction of CO<sub>2</sub>" *Angewandte Chemie Int.Ed.* **2010**, *49*, 6400.



- [31] W. Yang, J. Li, B. Liu, X. Zhang, C. Zhang, P. Niu, X. Jiang, "Multi-wavelength tailoring of a  $ZnGa_2O_4$  nanosheet phosphor via defect engineering" *Nanoscale* **2018**, *10*, 19039.
- [32] A. Bessière, S. Jacquart, K. Priolkar, A. Lecointre, B. Viana, D. Gourier, " $ZnGa_2O_4:Cr^{3+}$ : a new red long-lasting phosphor with high brightness" *Opt. Express* **2011**, *19*, 10131.
- [33] X. Hou, T. Xuan, H. Sun, X. Chen, H. Li, L. Pan, "High-performance perovskite solar cells by incorporating a  $ZnGa_2O_4:Eu^{3+}$  nanophosphor in the mesoporous  $TiO_2$  layer" *Sol. Energy Mater. Sol. Cells* **2016**, *149*, 121.
- [34] T. Maldiney, A. Bessière, J. Seguin, E. Teston, S. K. Sharma, B. Viana, A. J. J. Bos, P. Dorenbos, M. Bessodes, D. Gourier, D. Scherman, C. Richard, "The in vivo activation of persistent nanophosphors for optical imaging of vascularization, tumours and grafted cells" *Nat. Mater.* **2014**, *13*, 418.
- [35] T. Maldiney, B. Ballet, M. Bessodes, D. Scherman, C. Richard, "Mesoporous persistent nanophosphors for in vivo optical bioimaging and drug-delivery" *Nanoscale* **2014**, *6*, 13970.
- [36] H. Kawazoe, K. Ueda, "Transparent Conducting Oxides Based on the Spinel Structure" *J. Am. Ceram. Soc.* **2004**, *82*, 3330.
- [37] S.-H. Tsai, S. Basu, C.-Y. Huang, L.-C. Hsu, Y.-G. Lin, R.-H. Horng, "Deep-Ultraviolet Photodetectors Based on Epitaxial  $ZnGa_2O_4$  Thin Films" *Sci. Rep.* **2018**, *8*, 1.
- [38] Z. Lou, L. Li, G. Shen, "High-performance rigid and flexible ultraviolet photodetectors with single-crystalline  $ZnGa_2O_4$  nanowires" *Nano Res.* **2015**, *8*, 2162.
- [39] N. W. Grimes, "The spinels: versatile materials" *Physics in Technology* **1975**, *6*, 22–27; S. Mesoraca, S. Knudde, D. C. Leitao, S. Cardoso, M. G. Blamire, "All-spinel oxide Josephson junctions for high-efficiency spin filtering" *J. Phys.: Condens. Matter* **2018**, *30*, 015804.

- [40] J. Muro-Cruces, A. G. Roca, A. López-Ortega, E. Fantechi, D. del-Pozo-Bueno, S. Estradé, F. Peiró, B. Sepúlveda, F. Pineider, C. Sangregorio, J. Nogues, "Precise Size Control of the Growth of  $Fe_3O_4$  Nanocubes over a Wide Size Range Using a Rationally Designed One-Pot Synthesis" *ACS Nano* **2019**, *13*, 7716.
- [41] Y. Okamoto, S. Niitaka, M. Uchida, T. Waki, M. Takigawa, Y. Nakatsu, A. Sekiyama, S. Suga, R. Arita, H. Takagi, "Band Jahn-Teller Instability and Formation of Valence Bond Solid in a Mixed-Valent Spinel Oxide  $LiRh_2O_4$ " *Phys. Rev. Lett.* **2008**, *101*, 086404.
- [42] H. Peng, A. Zakutayev, S. Lany, T. R. Paudel, M. d'Avezac, P. F. Ndione, J. D. Perkins, D. S. Ginley, A. R. Nagaraja, N. H. Perry, T. O. Mason, A. Zunger, "Li-Doped  $Cr_2MnO_4$ : A New p-Type Transparent Conducting Oxide by Computational Materials Design" *Adv. Funct. Mater.* **2013**, *23*, 5267.
- [43] M. N. Amini, H. Dixit, R. Saniz, D. Lamoen, B. Partoens, "The origin of p-type conductivity in  $ZnM_2O_4$  ( $M = Co, Rh, Ir$ ) spinels" *Phys. Chem. Chem. Phys.* **2014**, *16*, 2588.
- [44] T. R. Paudel, A. Zakutayev, S. Lany, M. d'Avezac, A. Zunger, "Doping Rules and Doping Prototypes in  $A_2BO_4$  Spinel Oxides" *Adv. Funct. Mater.* **2011**, *21*, 4493.
- [45] Y. Xia, T. Wang, X. Zhao, X. Jiao, D. Chen, "Theoretical and Experimental Investigations on Effects of Native Point Defects and Nitrogen Doping on the Optical Band Structure of Spinel  $ZnGa_2O_4$ " *J. Phys. Chem. C* **2018**, *122*, 5509.
- [46] A. De Vos, K. Lejaeghere, D. E. P. Vanpoucke, J. J. Joos, P. F. Smet, K. Hemelsoet, "First-Principles Study of Antisite Defect Configurations in  $ZnGa_2O_4:Cr$  Persistent Phosphors" *Inorg. Chem.* **2016**, *55*, 2402.
- [47] A. R. Nagaraja, N. H. Perry, T. O. Mason, Y. Tang, M. Grayson, T. R. Paudel, S. Lany, A. Zunger, "Band or polaron: The hole conduction mechanism in the p-Type spinel  $Rh_2ZnO_4$ " *J. Am. Ceram. Soc.* **2012**, *95*, 269.

- [48] M. Dekkers, G. Rijnders, D. H. A. Blank, "*ZnIr<sub>2</sub>O<sub>4</sub>, a p-type transparent oxide semiconductor in the class of spinel zinc-d6-transition metal oxide*" *Appl. Phys. Lett.* **2007**, *90*, 021903.
- [49] Ray- Hua Hrong, Yu-Yuan Zeng, Wei-Kai Wang, Chia-Lung Tsai, Yi-Keng Fu, and Wei-Hung Kuo, "*Transparent electrode design for AlGaIn deep-ultraviolet light-emitting diodes*" *Optics Express* **2017**, *25*, 32206–13.
- [50] E. Chikoidze, A. Fellous, A. Perez-Tomas, G. Sauthier, T. Tchelidze, C. Ton-That, T. T. Huynh, M. Phillips, S. Russell, M. Jennings, B. Berini, F. Jomard, Y. Dumont, "*P-type β-gallium oxide : a new perspective for power and optoelectronic devices*" *Mater. Today Phys.* **2017**, *3*, 118.
- [51] E. Chikoidze, C. Sartel, H. Mohamed, T. Tchelidze, M. Modreanu, C. Vales-Castro, C. Rubio, C. Arnold, V. Sallet, Y. Dumont, A. Perez-Tomas, "*Enhancing the intrinsic p-type conductivity of the ultra-wide bandgap Ga<sub>2</sub>O<sub>3</sub> semiconductor*" *J. Mater. Chem. C* **2019**, 10.1039.C9TC02910A.
- [52] M. S. Relvas, M. R. N. Soares, S. O. Pereira, A. V. Girão, F. M. Costa, T. Monteiro, "*Trends in Cr<sup>3+</sup> red emissions from ZnGa<sub>2</sub>O<sub>4</sub> nanostructures produced by pulsed laser ablation in a liquid medium*" *J. Phys. Chem. Solids* **2019**, *129*, 413.
- [53] R. Al-Gaashani, S. Radiman, A. R. Daud, N. Tabet, Y. Al-Douri, "*XPS and optical studies of different morphologies of ZnO nanostructures prepared by microwave methods*" *Ceram. Int.* **2013**, *39*, 2283.
- [54] N. Winkler, R. A. Wibowo, W. Kautek, G. Ligorio, E. J. W. List-Kratochvil, T. Dimopoulos, "*Nanocrystalline Ga<sub>2</sub>O<sub>3</sub> films deposited by spray pyrolysis from water-based solutions on glass and TCO substrates*" *J. Mater. Chem. C* **2019**, *7*, 69.

- [55] D.-Y. Cho, "Chemical and structural properties of ternary post-transition metal oxide thin films: InZnO, InGaO and GaZnO" *Curr. Appl. Phys.* **2015**, *15*, 1337.
- [56] M. C. Biesinger, L. W. M. Lau, A. R. Gerson, R. St. C. Smart, "Resolving surface chemical states in XPS analysis of first row transition metals, oxides and hydroxides: Sc, Ti, V, Cu and Zn" *Applied Surface Science* **2010**, *257*, 887.
- [57] C. Li, J.-L. Yan, L.-Y. Zhang, G. Zhao, "Electronic structures and optical properties of Zn-doped  $\beta$ -Ga<sub>2</sub>O<sub>3</sub> with different doping sites" *Chinese Phys. B* **2012**, *21*, 127104.
- [58] D. Skachkov, W. R. L. Lambrecht, "Computational study of electron paramagnetic resonance parameters for Mg and Zn impurities in  $\beta$ -Ga<sub>2</sub>O<sub>3</sub>" *Appl. Phys. Lett.* **2019**, *114*, 202102.
- [59] N. Li, X. Duan, F. Yu, H. Jiang, "Effects of preparation method and temperature on the cation distribution of ZnGa<sub>2</sub>O<sub>4</sub> spinel studied by X-ray photoelectron spectroscopy" *Vacuum* **2017**, *142*, 1.
- [60] G. K. Wertheim, S. Hufner, "X-Ray Photoemission Band Structure of Some Transition-Metal Oxides" *Phys. Rev. Lett.* **1972** *28*, 4.
- [61] J. Xu, Y. Teng, F. Teng, "Effect of Surface Defect States on Valence Band and Charge Separation and Transfer Efficiency" *Sci. Rep.* **2016**, *6*, 32457.
- [62] B.J. Carey, J. Z. Ou, R.M. Clark, K.J. Berean, A. Zavabeti, A.S.R. Chesman, S.P. Russo, D.W.M. Lau, Z-Q. Xu, Q. Bao, O. Kavehei, B. C. Gibson, M. D. Dickey, R. B. Kaner, T. Daeneke, K. K-Zadeh, "Wafer-scale two-dimensional semiconductors from printed oxide skin of liquid metals" *Nat Commun* **2017** *8*, 14482.
- [63] M. Michling, D. Schmeißer, "Resonant Photoemission at the O1s threshold to characterize  $\beta$ -Ga<sub>2</sub>O<sub>3</sub> single crystals" *IOP Conf. Ser.: Mater. Sci. Eng.* **2012**, *34*, 012002.

- [64] F. Fuchs, J. Furthmüller, F. Bechstedt, M. Shishkin, G. Kresse, "Quasiparticle band structure based on a generalized Kohn-Sham scheme" *Phys. Rev. B* **2007**, 76, 115109.
- [65] A. Navarro-Quezada, S. Alamé, N. Esser, J. Furthmüller, F. Bechstedt, Z. Galazka, D. Skuridina, P. Vogt, "Near valence-band electronic properties of semiconducting  $\beta$ -Ga<sub>2</sub>O<sub>3</sub> (100) single crystals" *Phys. Rev. B* **2015**, 92, 195306.
- [66] J. B. Varley, J. R. Weber, A. Janotti, C. G. Van de Walle, "Oxygen vacancies and donor impurities in  $\beta$ -Ga<sub>2</sub>O<sub>3</sub>" *Appl. Phys. Lett.* **2010**, 97, 142106.

## Experimental details

### A. Thin-film Growth

Ga<sub>2</sub>O<sub>3</sub>, ZnO and ZnGa<sub>2</sub>O<sub>4</sub> samples were grown in a RF-heated horizontal metalorganic chemical vapour deposition MOCVD reactor with separate inlets to avoid premature reactions in the manifold between oxygen and organometallics precursors. The reactor can operate at low pressure, between 30 and 760 torr, and at high growth temperature, up to 1000 °C. Trimethylgallium (TMGa), diethylzinc (DEZn) and 5.5N pure oxygen were used as gallium, zinc and oxygen sources, respectively. Argon was used as carrier gas.

**Ga<sub>2</sub>O<sub>3</sub> and ZnGa<sub>2</sub>O<sub>4</sub>.** The TMGa and DEZn bubbler temperatures were fixed at -10°C and 0°C, respectively. ZnGa<sub>2</sub>O<sub>4</sub> layers were grown on C-oriented sapphire substrates. During the growth, the flow rate of TMGa and oxygen were kept at 11 μmol/min and 1200 sccm, respectively. The growth temperature was set at 775°C, the reactor pressure was 38 torr and growth time was 150 minutes. The DEZn flow was varied in the range (2.8-8.9 μmol/min). It were defined several reference pure β-Ga<sub>2</sub>O<sub>3</sub> samples without Zn (or Zn0) and several Ga-Zn-O specimens under the following conditions: 2,8 μmol/min (Zn3), 3,9 μmol/min (Zn4), 5 μmol/min (Zn5), 7 μmol/min (Zn7), 8,9 μmol/min (Zn9).

**ZnO.** ZnO films were grown on *c*-oriented sapphire substrates. During the growth, the flow rate of DeZn and nitrous oxide (N<sub>2</sub>O) were kept at 20 μmol/min and 3700 sccm, respectively. The growth temperature was fixed at 950°C, the reactor pressure was 50 torr. The growth rate was 280 nm/h in this growth conditions.

## **B. Characterization Methods**

**B.1. XRD.** X-ray diffraction profiles were recorded in  $\theta/2\theta$  configuration, using Rigaku SmartLab equipped with Cu-K $\alpha$ 1 source ( $\lambda=0,1541\text{nm}$ ).

**B.2. Raman Spectroscopy.** Raman spectra were acquired in a Witec spectrometer coupled to a 488.0 nm laser excitation. The laser was focused on the sample by a 50 $\times$  objective with a 1 mW power. We used a 600 g/mm grating, covering a spectral window from 100 to 4000  $\text{cm}^{-1}$  with a spectral resolution of 3  $\text{cm}^{-1}$ /pixel. Single Raman spectra of 60 seconds were registered.

**B.3. Transmittance/Reflectance.** Optical transmission spectra were measured in 200-2000 nm spectral range with a Perkin Elmer 9 spectrophotometer.

**B.4. SEM/EDX.** SEM images were done by FEG JEOL 7001-F electron microscopy, which is equipped with Everhart-Thornley detector of secondary electrons. EDX analyses have been carried out by EM FEG OXFORD machine with SSD X-MAX detector.

**B.5. TEM/EDX/EELS.** Crystallographic characterization and imaging were conducted using a field emission gun FEI Tecnai F20 microscope at 200 kV with a point-to-point resolution of 0.24 nm. Energy dispersive X-ray (EDX) and electron energy loss spectroscopy (EELS) spectrum images and profiles were obtained in high angle annular dark-field (HAADF) STEM mode with an EDAX super ultra-thin window (SUTW) X-ray detector and a Gatan Quantum SE 963 imaging filter respectively. TEM cross-sections were prepared by conventional mechanical polishing and ion milling.

**B.6. XPS.** X-ray photoemission spectroscopy (XPS) measurements were performed with a Phoibos 150 analyzer (SPECS GmbH, Berlin, Germany) in ultra-high vacuum conditions (base pressure  $3 \times 10^{-10}$  mbar). XPS measurements were performed with a monochromatic Al K $\alpha$  X-ray source (1486.74 eV). The main ZnGa<sub>2</sub>O<sub>4</sub> Ga2*p* and Zn2*p* peak energies were consistent with previous literature after adventitious C1s calibration (284.8 eV). The C1s calibration shift for the reference ZnGa<sub>2</sub>O<sub>4</sub> was only of 0,595 eV. The C1s calibration shift energies were also relatively small for the other specimens with -0.3 eV and 2,8 for reference (*n*-type) ZnO and (highly resistive) Ga<sub>2</sub>O<sub>3</sub>, respectively.

**B.7. Transport.** Hall Effect measurement set-up. Ohmic contacts were prepared by silver paint at the four corners of the sample. Hall Effect measurements were performed in a Van der Pauw configuration in the temperature range of 300 K to 850 K and for magnetic fields perpendicular to the film plane varying from -1.6 T to 1.6 T, using a high impedance measurement set-up which was custom designed for measurement of high resistance.

### C. Ab-initio Methods

For the hexagonal ZnO cell containing 2 Zn atoms and 2 oxygen atoms. The lattice constants are:  $a = b = 3.249$  Å,  $c = 5.207$  Å. The generalized gradient approximation with the mean-field Hubbard correction (GGA+U), together with the Perdew-Burke-Ernzerhof functional (PBE), cut-off energy of 140 Hartree and  $23 \times 23 \times 13$  *k*-points grid were used for the simulation. The U parameters are set to 4 eV and 9.5 eV for O2*p* and Zn3*d* respectively. For the face-centered cubic ZnGa<sub>2</sub>O<sub>4</sub>, local density approximation with semi-empirical approach (LDA-1/2) was used in the simulation. *k*-points sampling are set to  $20 \times 20 \times 20$ , and the lattice constant is  $a = b = c = 8.338$  Å. For the monoclinic  $\beta$ -Ga<sub>2</sub>O<sub>3</sub>, Meta\_GGA (one of semi-local approximations functionals, an alternative of the DFT-1/2) was used in the simulation. The *k*-points



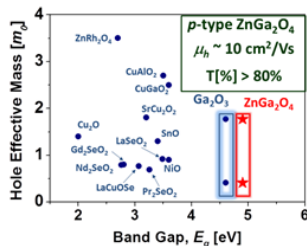
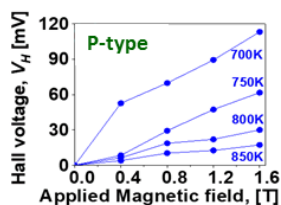
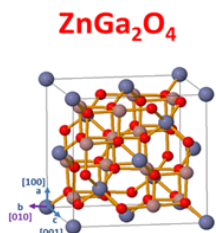
sampling was set to  $4 \times 8 \times 8$ , and the monoclinic cell contains 16 Ga atoms and 24 O atoms. The lattice constants are:  $a = 12.23 \text{ \AA}$ ,  $b = 6.08 \text{ \AA}$ ,  $c = 5.8 \text{ \AA}$ , and  $\beta = 103.7^\circ$ .

For the  $\text{ZnGa}_2\text{O}_4$  antisite pair DFT simulations, a 112-atom supercell was built ( $\text{Zn}_{16}\text{Ga}_{32}\text{O}_{64}$ ). The calculation was conducted with the Quantumwise software. The antisite model was firstly optimized geometrically using the GGA PBE functional. The optimized model was then calculated with a  $4 \times 4 \times 4$   $k$ -point grid using the meta-GGA method. The  $c$  parameter was chosen as 1.45 to match with the experimental bandgap of the  $\text{ZnGa}_2\text{O}_4$  host. Density mesh cut-off was set to 125 Hartree, and the broadening was set to 25 meV, which had the energy convergence up to  $1 \times 10^{-4}$  eV.

# *P*-type ultra-wide bandgap spinel ZnGa<sub>2</sub>O<sub>4</sub>: new perspectives for energy electronics

Ekaterine Chikoidze, Corinne Sarte, Ismail Madac, Hagar Mohamed, Christele. Villar, Belén Ballesteros, Francisco Belarr, Elena del Corro, Pablo Vales-Castr, Guillaume Sauthier, Lijie Li, Mike Jennings, Vincent Salle, Yves Dumont and Amador Pérez-Tomás

## Spinel Bipolar Electronics



**ZnGa<sub>2</sub>O<sub>4</sub> *p*-type widest bandgap ternary oxide**

We have demonstrated that Ultra-wide band gap (~5 eV) spinel zinc gallate (ZnGa<sub>2</sub>O<sub>4</sub>) is the native *p*-type ternary oxide semiconductor. This is important step towards *p*-type doping, opens up further perspectives for ultra-wide bandgap *bipolar spinel electronics* to be integrated into the next generation more efficient energy optoelectronics and power electronics.

